A LOWER-LIMB EXOSKELETON EMULATOR TO

BE EMPLOYED IN ESTIMATION OF HIP

IMPEDANCE IN NORMAL GAIT

by

Jason Y. Lee

A thesis submitted to the Faculty and the Board of Trustees of the Colorado School of Mines in partial fulfillment of the requirements for the degree of Master of Science (Mechanical Engineering).

Golden, Colorado

Date _____

<div style="text-align: right">

Signed: _____

Jason Y. Lee

Signed: _____

Dr. Ozkan Celik
Thesis Advisor

</div>

Golden, Colorado

Date _____

<div style="text-align: right">

Signed: _____

Dr. Greg Jackson
Professor and Head
Department of Engineering

</div>

ABSTRACT

Recent progress in robotic control and technology has contributed to an increase in interest and applications of wearable robotics, also known as exoskeletons. Identification of exoskeleton mechanical and control parameters that will provide the best performance for specific tasks remains as a significant challenge. Exoskeleton emulators, which allow real-time adjustment of device parameters (such as stiffness of an emulated spring) have emerged as valuable tools that enable fast, iterative experimentation and testing.

This thesis presents design, implementation, and characterization results of a lower-limb exoskeleton emulator system with offloaded actuation. The emulator is able to apply controlled torques in the ankle, knee and hip joint sagittal degrees of freedom through five braces that were developed. A PID controller was implemented for the emulator to control the torques applied at the brace joints.

Characterization of hip joint impedance is essential to the groundwork for design and control system of exoskeletons, orthoses, and prostheses. A pilot test with a single healthy subject was conducted, using the emulator as a perturbation source and focusing on identification of hip impedance parameters during normal walking. A model, that incorporated stiffness, damping, and inertia parameters as polynomial coefficients, was used to calculate the impedance values from the collected data. The results showed that the perturbation amplitudes were inadequate and soft tissues at the leg attachment points prevented effective delivery of the torques to the leg. Future work on impedance estimation of hip will focus on improving brace leg attachments and enhancing the delivered torque.

In conclusion, an exoskeleton emulator for the lower-limb was successfully designed, constructed, characterized, and tested. The exoskeleton emulator will enable a variety of future studies on gait augmentation and assistance.

TABLE OF CONTENTS

LIST OF FIGURES AND TABLES

LIST OF SYMBOLS

Desired Brace Torque . . . . τ_{Des}

Motor Position . . . . θ_m

Brace Position . . . . θ_b

Polynomial Coefficients . . . . A,B,C,D

Desired Motor Position . . . . $\theta_{m,Des}$

Actual Motor Position . . . . $\theta_{m,Act}$

Electrical Motor Current . . . . I_m

Controller Error . . . . $e(t)$

Proportional Gain . . . . K_p

Integral Gain . . . . K_i

Derivative Gain . . . . K_d

Resultant Hip Joint Angle profile . . . . θ_r

Resultant Hip Joint Velocity profile . . . . $\dot{\theta}_r$

Resultant Hip Joint Acceleration profile . . . . $\ddot{\theta}_r$

Average Perturbation Torque . . . . τ_p

Total Inertia of Hip . . . . I_t

Damping Values of Hip . . . . b_h

Stiffness Values of Hip . . . . k_h

LIST OF ABBREVIATIONS

Energy Storage and Return . . . . ESR

Degree of Freedom . . . . DOF

Proportional-Integral-Derivative . . . . PID

Estimated Stride Time . . . . EST

ACKNOWLEDGMENTS

I would first like to thank my thesis advisor Dr. Ozkan Celik for consistently providing guidance and support for the exoskeleton emulator project. He has always been available for all research questions and has continually helped troubleshoot our system. I also want to thank my committee members Dr. Anthony Petrella and Dr. Anne Silverman for introducing me to and teaching me biomechanics. They have been great mentors and have constantly given recommendations and feedback to this project.

I would like to thank undergraduate students Nick Collins and Megan Auger for their hard work and dedication. They have willingly sacrificed their own time, energy, and effort to help design, manufacture, program, and conduct experiments.

I want to thank my parents, my sister, and my whole family for providing me with unequivocal love, support and encouragement throughout my years of study and through the process of researching and writing this thesis. I would not have accomplished this much in my life without them.

Finally, I must express my very profound gratitude to another graduate student, Kyle Heer, who has worked alongside me my whole Masters career to complete the exoskeleton emulator. He has demonstrated the highest level of dedication, determination, and work ethic required to complete this project in a timely manner. He has taught me to take great pride in my work, and I would not have completed this project without him. Thank you.

CHAPTER 1

INTRODUCTION

The hip joint is vital to human locomotion. Walking is a part of everyday life and provides humans with their primary mode of transportation. Losing the ability to walk, due to neurological disorders such as stroke, substantially limits the functional independence of individuals.

This thesis aims to establish initial stages of a longer term research effort, which will focus on development and testing of a passive bilateral lower extremity exoskeleton that will enable energy storage and return across the paretic and non-paretic leg joints of hemiparetic stroke survivors. This section provides a description of the research motivation and objectives of this thesis in further detail.

1.1 Research Motivation

Understanding the dynamic mechanical properties (impedance) of the hip joint during gait is imperative for development and control of assistive or rehabilitative exoskeletons and orthoses. Even though impedance of ankle and knee joints have been studied in various contexts, primarily driven by the need to inform prosthesis design and control, impedance of the hip has remained mostly unexplored [1–8]. Passive exoskeletons, or exoskeletons that enable energy storage and return (ESR) across joints, would particularly benefit from characterization of hip impedance, due to the need to properly tune stiffness of springs used in ESR. Such exoskeletons can be used to make walking more efficient (i.e. decrease metabolic cost) in healthy individuals, or provide assistance to the impaired leg joints of hemiparetic

stroke survivors, using energy stored from their unaffected leg, by collecting energy during the negative work portion of the gait cycle and applying energy at the most concentrated phase of positive work.

Energy storage and return (ESR) can be applied at any lower extremity joint [9]. ESR has been proven to be effective in reducing metabolic cost of walking using a passive ankle exoskeleton where metabolic energy was reduced up to 7.2% [10]. Currently, ESR is applied to a single joint, but there are opportunities to apply ESR to multiple joints. It is also possible to store energy from one leg and transfer the this energy to the opposite leg. Using ESR between bilateral joint pairs can particularly aid in gait assistance and rehabilitation of hemiparetic stroke survivors.

A hip exoskeleton can also help in the realm of running and sprinting efficiency. In walking, it is known that the ankle joint contributes the majority of the positive work ($\sim$53% of total positive work), while in sprinting the hip joint flexion/extension contributes the most work at 49% [11]. There are multiple applications for running and sprinting aids including the military, law enforcement, and fire departments where high mobility is required.

1.2 Research Objective

This thesis project has two goals. The first goal is design and implementation of an exoskeleton emulator that is capable of applying accurately controlled torques to hip, knee and ankle joints of human subjects during walking and running. The second goal is identification of hip impedance during walking of a healthy individual, using the said exoskeleton emulator to provide torque perturbations during experiments. A pilot test was conducted to obtain preliminary results and evaluate the procedural steps, feasibility and data collection

and analysis methods. Completion of these two goals will inform and enable future studies that will focus on development of a passive ESR bilateral hip exoskeleton that will recycle energy between the hip joints to aid stroke patients.

This thesis starts with a review of literature on hip exoskeletons and exoskeleton emulators. This is followed by an overview of the completed design and integration of the exoskeleton emulator in this project as well as the control system. Lastly, a description of the pilot test that consists of the experimental protocol, data analysis, and results on hip impedance estimation is presented.

CHAPTER 2

BACKGROUND

There have been many studies on use of exoskeleton technology, ranging from load carrying, strength or endurance augmenting exoskeletons for military purposes [12, 13], to exoskeletons that provide assistance to motor-impaired or elderly populations [14–18]. Despite the fact that active hip joints are commonly used in these exoskeletons, there has been a gap of knowledge in characterization of hip impedance during gait, which can inform design of hip motor augmentation or assistance controllers. This literature review first summarizes use of exoskeletons in assisting stroke survivors and improving walking energetics for healthy individuals. Then it focuses on passive exoskeletons and leg joint impedance, with specific focus on existing studies on hip joint impedance characterization. Finally, it concludes with the motivation behind building an exoskeleton emulator.

2.1   Stroke and Assistive/Rehabilitative Exoskeletons

Roughly 7,000,000 Americans above the age of 20 years have suffered a stroke and are living with related disabilities, while an estimated 795,000 Americans have a new or recurring stroke each year [19]. In the United States stroke is the main cause of long-term disability where 50% of ischemic stroke survivors over the age of 65 years have hemiparesis [19]. Lower extremity exoskeletons have been suggested and developed to aid mobility and rehabilitation of stroke patients [20]. There is evidence that exoskeletons can help post-stroke patients sustain a more symmetric gait, but they have limitations when used as a device to aid in activities of daily living and there are areas open to improvement to optimize performance

[21]. These limitations include battery dependence and bulky/heavy structures. Ultimately, hip impedance can inform development and design of a lightweight passive exoskeleton that can assist in gait rehabilitation and serve as a body-powered mobility aid.

2.2 Exoskeletons for Metabolic Cost Reduction in Healthy Individuals during Walking and Running

Following the fact that running and sprinting use more hip joint power than the the ankle and knee joint, there has been research on soft exoskeletons that span multiple joints that have demonstrated that assisting hip extension during walking can benefit walking efficiency by leading to an average metabolic reduction of 4.6% [22]. The same research team has also contributed a hip only exoskeleton design with an IMU (inertial measurement unit)-based iterative control and reported metabolic energy savings from 5.7% to 8.5% during walking trials [23]. The timing of energy delivery in the gait cycle is shown to be important to optimize metabolic energy savings because applying energy at arbitrary times may obstruct natural gait [24].

2.3 Passive Exoskeletons

There are two types of exoskeletons, based on whether it uses an external energy source or not and termed as active and passive exoskeletons, respectively. Active exoskeletons are powered orthoses that commonly require electrical power for motors and other electrical devices that provide the torque necessary for lower limb joints throughout the gait cycle [20, 25–27]. Despite the actuation capabilities of active exoskeletons, several disadvantages stem from heavy inertia of the motors, gearboxes, the battery and the structure required to carry these components. The significant additional inertia leads to metabolically inefficient

walking. Depending on the torque output employed on the joint, the added mass can cancel out the metabolic energy savings or even increase the net metabolic cost. Another crucial downside is the power supply that can hinder the portability of the device due to its added mass and limited active usage time [9].

Passive exoskeletons are classified as rigid apparatuses that use passive elements, such as springs and clutches to create assistive joint torques. The elastic elements are represented as springs while the clutches can be powered or non-powered. Powered variable spring stiffness modules and clutches grant passive exoskeletons the ability to activate at any time and have a fast response for numerous spring stiffness, and ESR via a clutch [28, 29]. Figure 2.1 displays an example of a semi passive ankle exoskeleton with a clutch that is capable of instantaneous spring stiffness modifications [28]. Passive exoskeletons are lightweight, inexpensive, portable, and do not have a limited usage time or range due to not depending on batteries / external power sources [9]. Passive exoskeletons have mainly been in development towards the ankle joint since a large portion of work is concentrated at the push off phase during walking [9, 10, 28]. We desire to use a similar approach but instead focus on the hip joint. Data has shown the possibility of harnessing energy during walking, running, and sprinting when the hip goes into hip extension during the stance phase (when one leg is engaged with the ground and the opposite leg is swinging) [11]. If energy can be stored during this phase of the gait cycle, it can be released to add positive work at an opportune moment of hip flexion on the opposite hip.

For all exoskeletons, alignment of anatomical joint axes with the center of rotation of the exoskeletons' axes is a common technical challenge [30]. In rigid exoskeletons, the torque applied on the exoskeleton will directly impose a torque on the targeted joint, while soft

exoskeletons cover the span of the muscular tendons [22]. The direct physical application of torque transfer from the exoskeleton to the wearer has been the primary reason to pursue a rigid exoskeleton design in this project.
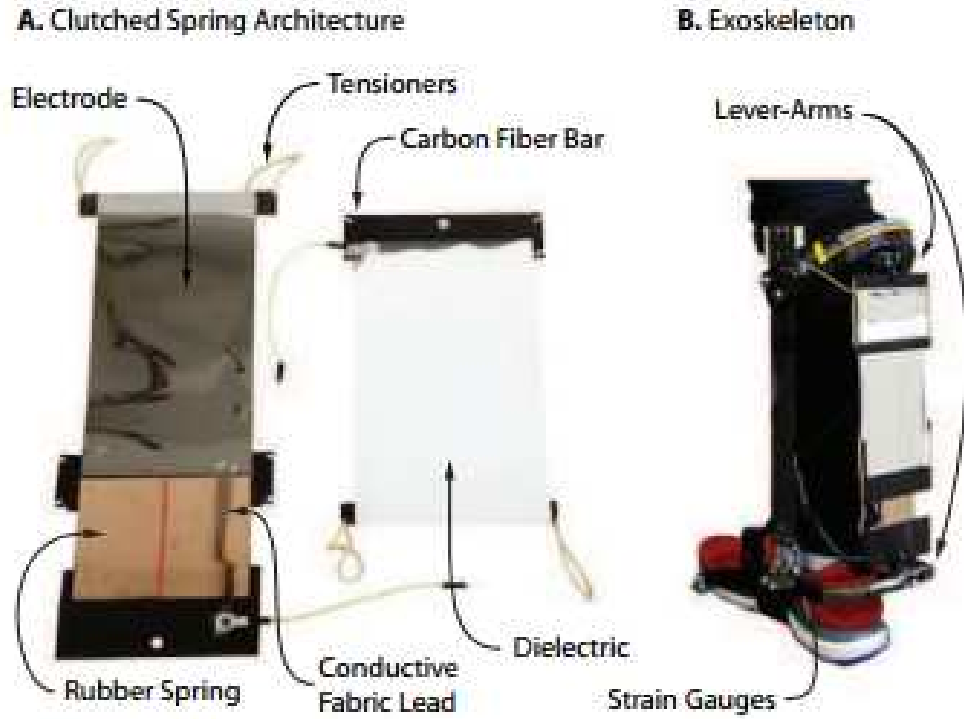

Figure 2.1: Example of Passive Ankle Exoskeleton
Passive ankle exoskeleton that contains a powered clutch and variable spring stiffness device (image from [28]). The clutch contains layers of electrodes that are divided by dielectric insulators that can independently activate any number of electrode panels to generate various stiffness effects when current is applied.

2.4 Hip Impedance

Joint impedance is valuable to the design and development of biomechatronic systems. One of the problems to be addressed in passive exoskeleton design is understanding the joint stiffness at different points of the gait cycle. Overall, research on joint impedance has primarily focused on the knee and ankle joints. There have been two common methods researchers have used to measure impedance. One method involves using a perturbation

7

robot or exoskeleton that can create an unexpected disturbance in the joint during gait to measure the effective stiffness of the joint [1, 6, 31]. A limitation of this method is that it captures data for only a portion of the gait cycle and experiments are conducted at a fixed walking speed. Without a treadmill it is difficult to regulate the walking speed. Futhermore, with a force plate the kinetics data may not be natural due to the subject adjusting walking speed and stride length to step on a force plate. The second method utilizes modeling techniques paired with electromyography (EMG), kinematics and kinetic data collection to correlate muscle force (estimated through musculoskeletal simulations) to joint position [32, 33]. Joint stiffness obtained using this method is termed "quasi-stiffness" to refer to the fact that several simplifications and assumptions are used in the model. Verifying the quasi-stiffness values or obtaining the actual stiffness values still requires experimental impedance data obtained via perturbations. Since quasi-stiffness of the hip varies during walking, it would be implied that actual joint stiffness would vary as well [34]. Regardless, a majority of the work in literature on joint impedance characterization during gait has focused on ankle and knee joints, leaving a gap of knowledge in hip joint impedance.

Several studies focused on ankle, knee, and hip stiffness characterization using the quasi-stiffness method [2, 7, 8, 34]. Figure 2.2 shows an estimate of hip quasi-stiffness [34]. Hip quasi-stiffness is largest at maximum extension which is expected since that is when the hip exhibits its highest work rate [9]. In [34], quasi-stiffness was calculated by estimating a linear slope of the moment-angle graph of the targeted joint. There is a difference between quasi-stiffness and actual stiffness which was studied by using a simple impedance controlled inverted pendulum model. The quasi-stiffness differs from actual stiffness in terms of active joints, and are similar in the passive joints [35]. Since active prostheses and orthoses fall in

8

the realm of powered joints, it is important to identify the actual stiffness of the joints they
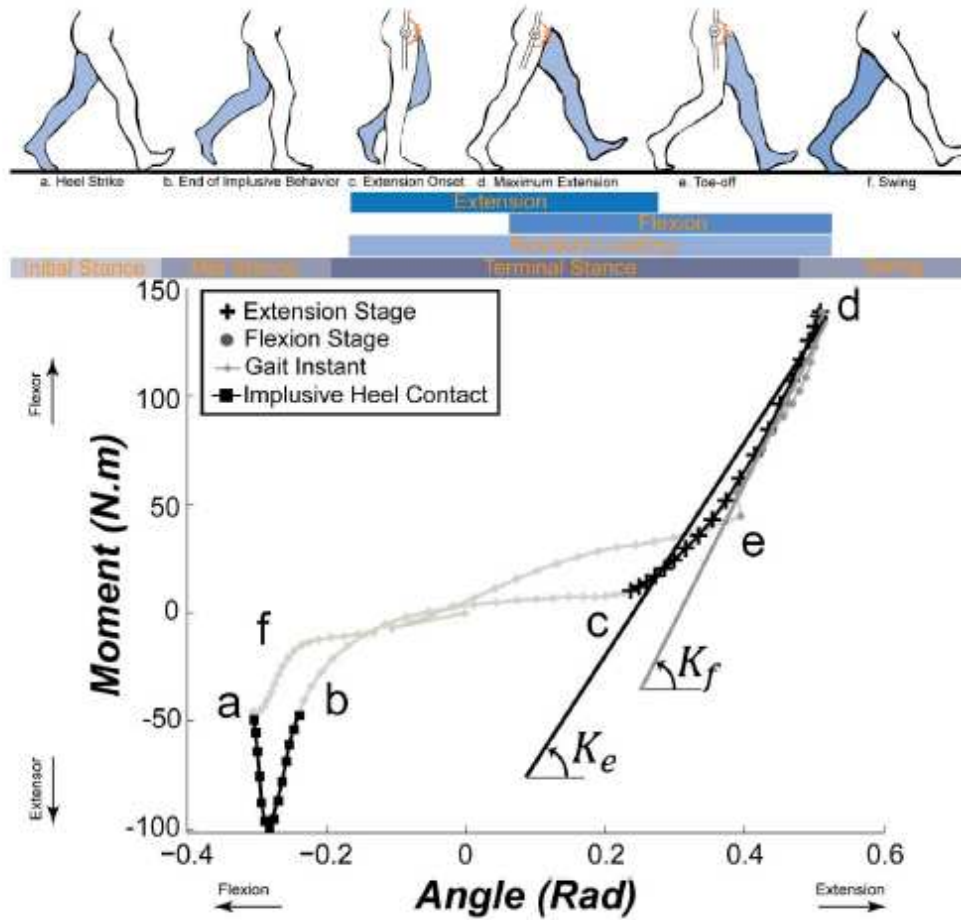
replace or assist.

Figure 2.2: Hip Quasi-Stiffness
Estimation of hip quasi-stiffness of subjects walking at speeds of $0.75 - 2.63$m/s (image from
[34]). Letters a-f represent the different phases of the gait cycle which is displayed for the
right (white color) leg. Ke and Kf are the linear fit of quasi-stiffness for the extension stage
(c - d) and flexion stage (d - e) of the loading phase of the hip, respectively.

There are two studies on the stiffness of the hip, which followed the quasi-stiffness method and used a gait trainer robot named LOPES [31, 34]. The goal of my thesis project is to obtain the actual hip stiffness, during both swing and stance phases of gait. The quasi-stiffness results from the literature provide an opportunity for comparison and discussion.

One of the downsides of the LOPES gait trainer exoskeleton is that the added mass of using a full lower extremity exoskeleton causes added inertia during the swing phase. Secondly, the perturbations were not induced during walking but at set leg orientations. Also, there was a study that tested ankle joint impedance at fixed walking speeds, which is relevant in everyday mobility, but since kinematics and kinetics differ between walking and running, it would imply that joint stiffness would change based off of different speeds [1]. A treadmill was used to control the constant speed of walking.

2.5   Exoskeleton Emulator

Building emulators is a recent approach in designing prosthetics and exoskeletons. Emulators in the literature have mainly focused on the ankle joint, but there have been other studies using a soft exoskeleton which targeted multiple joints that included the hip joint [23, 36–40]. The main motivation behind having an exoskeleton emulator is that it is a research tool that can simulate various types of exoskeletons (both passive and active) and controllers, without a substantial addition of inertia on the user. Typically, the emulator consists of an actuation cart and an exoskeleton/prosthetic wearable device that attach to each other via Bowden cables. The actuation cart is a mechatronic system that contains motors, amplifiers, power supplies, and a computer. The wearable device design is arranged to have Bowden cable connection in order for the tension of the cable to apply a torque around

10

the desired joints. Furthermore, there are sensors that measure force and angular position, embedded to the exoskeleton device to provide feedback to the controller [23, 36–40]. This allows for a range of torques that can be applied to the user without substantial additional weight. The emulator has the capability of implementing any type of control system so that many types of active or passive control scenarios and parameters can be tested. The main strength of an exoskeleton emulator is that it allows the user to test most any type of exoskeleton without the need of prototyping and individual designs. The exoskeleton emulator can, more importantly for this study, provide perturbations to the user. In addition to studying hip impedance, it was in the interest of Biomechatronics Research Laboratory to construct a full lower extremity exoskeleton emulator that can be used as a research tool, as it enables additional other studies.

CHAPTER 3

EXOSKELETON EMULATOR DESIGN

A full lower-extremity exoskeleton emulator was designed and created to answer questions that are relevant to the research of the Biomechatronics Robotics Laboratory (BRL). The exoskeleton is composed of five braces that span the ankle, knee, and hip. Although this thesis research question involves the joint identification of the hip, the ankle and knee brace were also built to allow numerous possibilities of experiments that can focus on single or multiple joints (such as ESR across multiple joints). The braces were manufactured in a machine shop mainly using a HaasCNC 3-axis mini-mill. In total the exoskeleton brace is composed of more than 160 machined parts. The following sections will provide more details of the design, hardware, and assembly of the device.

3.1   Exoskeleton Brace Frame

The main design goal for the exoskeleton was to maintain a safe, light, compact design that incorporates ease of attachment and adjustments on the wearer. The total width, height, and length of the brace were determined by observing anthropometric reference data of human adults that ranged in the 95th percentile range [41]. The frame is built from aluminum for low weight and durability. 0.5" diameter round hollow rods were used as the skeletal structure of the exoskeleton. The skeletal structure of the braces are arranged to be aligned parallel to the lower extremity and the lower torso of a human user. The length of the rods were calculated by observing the human anthropometric reference for the lower body [41]. Squared aluminum components were designed with a 0.501" circular through-

hole with an intersecting 3/32" wide slit for insertion of the rods. A 6-32 button socket head screw could be tightened perpendicular to the slit to grant compression of the through-hole for a secure and fixed position. Since the squared components can also rotate around the rods, both the rods and squared components have a 1/32" width marking to ensure that all the squared components are either parallel or perpendicular in respect of each other. This marking aligns with the length of the rods and are either set 90° or 180° apart on the circular cross section. The squared components typically have the alignment marking on opposite sides that run parallel to the slit. Each squared components have the capability of sliding along the rod and function as the attachment points of the human-exoskeleton cuffs, Bowden cable, and rods.

3.2 Human-Exoskeleton Attachment

Three different types of human-exoskeleton attachment components are employed: lower torso cuffs, thigh and shank cuffs, and sandal attachment (Figure 3.1). The lower torso cuffs have two brackets that are connected via an adhesive to 1 inch memory foam to provide comfort and better conformity to the body. These cuffs allow adjustability in the superior/inferior and medial/lateral directions for a better fit of the torso. Because the thigh and shank cuffs would occupy the most body composition of the lower body, a slim PVC pipe is chosen as the main member of the cuffs due to its flexible properties. Plastazote medical foam adheres to the inner walls of the cuffs for improved attachment and to reduce slippage. A simple adjustable Velcro strap is used to wrap the brace to the body. Several thigh and shank cuff sizes were created to accommodate a larger pool of test subjects. The sandal attachment is comprised of a commercial sandal with the common Velcro straps coupling

and is adapted with two horizontal parallel rods that are inserted in the sole. These rods are press fit to a C-shaped part that ultimately connects to the ankle brace. Multiple size shoe sandals will undergo the same modifications to fit a various range of test subjects foot size.

Figure 3.1: Human-Exoskelton Attachment Components
(Left view) lower torso cuffs. (Middle view) thigh and shank cuffs. (Right view) sandal attachment.

3.3 Exoskeleton Joint Design

The exoskeleton has four passive joints that span the hip and ankle braces; the passive joints are located posterior to the body. No torque or power is applied to the passive joints, instead they allow free motion in the inversion/eversion and abduction/adduction degrees of freedom for ankle and hip, respectively. There are six powered joints that have pulleys and a rotary encoder (E2-1250-250-IE-H-D-3, US DIGITAL) attached to the distal ends of axes to apply torque and measure joint angles (Figure 3.2). The pulleys are designed for simultaneous bi-directional actuation capability that allows flexion/extension torques. The powered joints apply torques in the sagittal plane and are placed lateral to the body. These

14

joints are designed to use the axle to align with the individual joints. For all joints, a 1/4"
stainless steel shaft is first press fit through a single bearing tab and then sandwiched between
two lubricated radial bearings that are press fitted into bearing tabs. The two outer tabs
are attached to the proximal segment and the single tab stacked in the middle is connected
to the distal segment. The pulley is fixed to the single tab by another 3/16" stainless steel
rod that couple to the pulleys rim. The rotary encoder disk is secured to the axle, and the
encoder sensor is fixed to the proximal segment. The design of the complex structure of the
distal and proximal tabs in combination with the additional axle of the distal tab provide
a natural mechanical hard stop. The hard stops are placed to limit motion beyond normal
anatomical ranges of motion and to prevent injury.
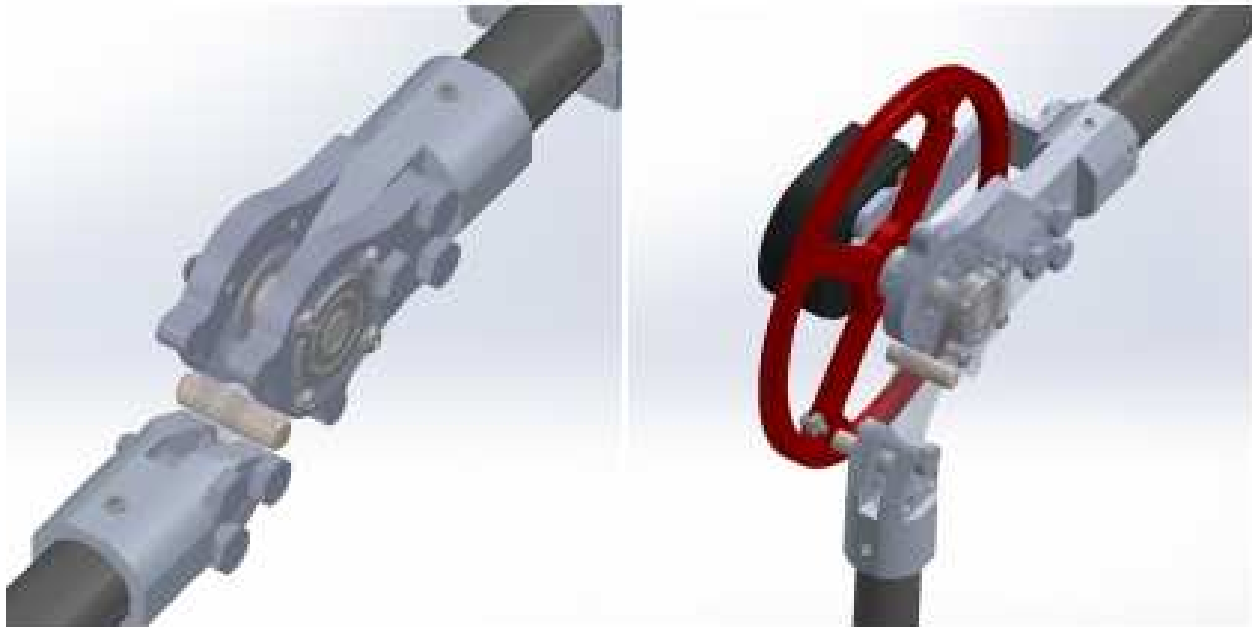
Figure 3.2: Brace Joints
Hard stops are incorporated to limit range of motion. (Left) passive joints allows freedom of
motion in the frontal plane. (Right) powered joints contains an attached pulley and encoder
and torques are applied in the saggital plane.

3.4 Brace Cable-Pulley Transmission

The Bowden cable termination block's main purpose is to conjoin the distal end of the Bowden sheath to the exoskeleton braces. This block is designed with a circular hole that the distal end Bowden cable capsule fits in. With the function of the slitting slot intersecting the circular hole allows a set screw to firmly fix the Bowden sheath in the block. Once attached, the Bowden termination blocks are angled in order for the Bowden cable to align tangential to each pulley. The block connects the end of the Bowden sheath to the brace and creates a linear path for the cable to connect to the pulley. This block can be repositioned to align tangentially to the pulley to either apply torque in the flexion or extension rotation. A Futek model LSB200 S-Beam Junior Load Cell is pulled in series with a Bowden cable and attaches to both the brace pulley and actuation cart motor pulley. The proximal Bowden cable is tied around the eye-hooks that screw into the load cell. The distal Bowden cable is secured to the pulley via set hex head screw and nut. To reduce slack around the pulley, the cable connects directly to the terminal point and does not fully wrap around the pulley. Figure 3.3 displays a description of the distal end of the Bowden cable attaching to the hip brace and displaying the transmission of torque.

3.5 Hip Brace

The hip exoskeleton, shown in Figure 3.4, consists of two lower torso cuffs and four thigh cuffs. The hip exoskeleton's mass is 2.33kg and it houses 2 degrees of freedom (DOF) for each leg: abduction/adduction and flexion/extension. The abduction/adduction hip joint is passive and allows a range of 40° abduction and 30° adduction while flexion/extension is an active joint with 120° flexion and 15° extension.
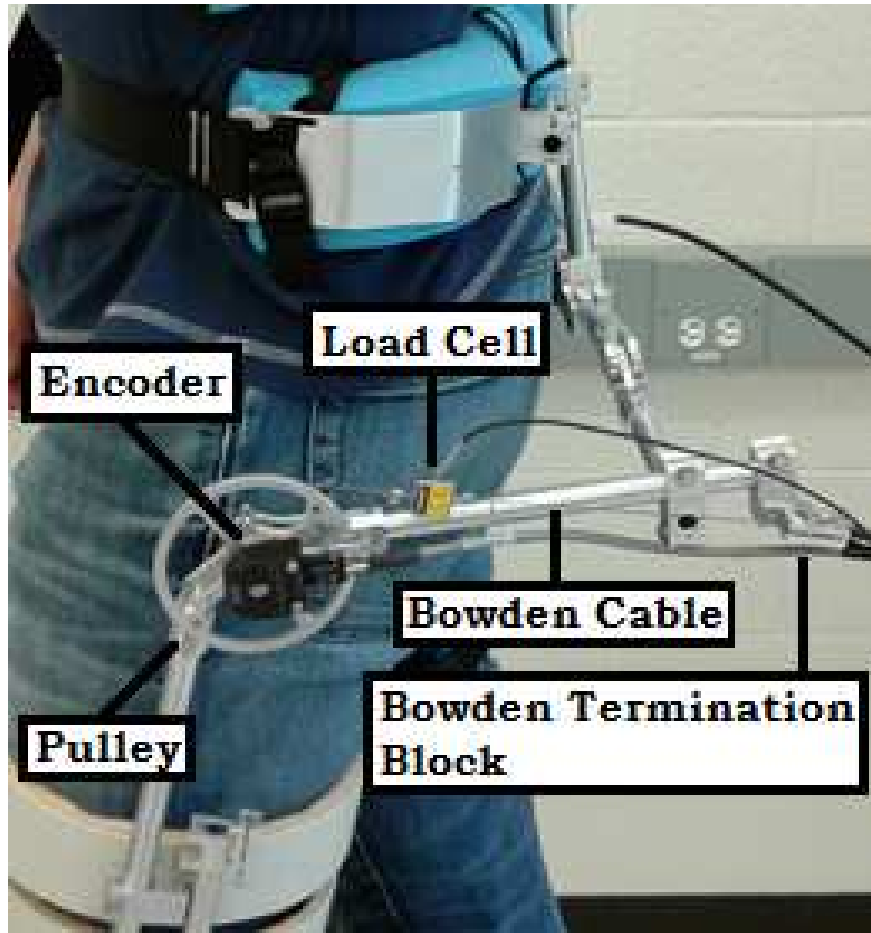
Figure 3.3: Hip Brace Transmission System

The Bowden cable is routed through the Bowden termination block and attaches to the force sensor then connects to the pulley. The force sensor and encoder have ease of connection and disconnection in case of different cable routes.

These joints are designed for their axes of rotation to intersect at the hip center of rotation for better human-machine alignment. Design complexity would intensify with the addition of an internal/external hip rotation DOF and since research is focused on the sagittal plane of the human motion, this DOF was left out. There are two pulleys designed to be aligned with the center of rotation of the hip in the sagittal plane. The pulleys are designed for simultaneous bi-directional actuation capability that apply torque for hip flexion/extension motion. The diameter of the pulleys is 83.3mm. Four Bowden termination blocks can be used to allow simultaneous bi-directional motion of each hip pulley. There is a total of 25 passive adjustment points that can easily be locked and unlocked to best conform the exoskeleton to the human operator. These adjustment points include the squared components and the velcro straps from the attachment mechanisms.

3.6   Knee Brace

Each knee brace contains two thigh cuffs and two shank cuffs (Figure 3.5). The two thigh cuffs and one of the shank cuffs have approximately the same circumference. The two shank cuffs have a different circumference due to the size constraint of the human calf and the reduction in the human shank size distal of the calf. Each knee brace has a mass of 0.54kg. The knee brace holds one DOF which is a powered joint that allows flexion/extension with a range of motion of 135°. There are 9 adjustment points that have easy access because all of the points are in the sagittal plane.

Figure 3.4: Completed Hip Exoskeleton

Figure 3.5: Completed Knee Exoskeleton

3.7   Ankle Brace

Each ankle brace consist of two shank cuffs and the sandal attachment (Figure 3.6). The cuffs arrangements are the same as the knee proximal segment cuffs. The individual ankle brace have a mass of 1.05kg and grants two DOFs: dorsiflexion/plantarflexion and inversion/eversion. The dorsiflexion/plantarflexion joint is active and allows a range of 20° dorsiflexion and 50° plantarflexion while inversion/eversion is a passive joint with 15° inversion and 20° eversion. Unlike other exoskeleton designs that may allow inversion/eversion but do not align with the center of rotation, this ankle brace is structured to have both joint axes to intersect with the center of rotation of the ankle to allow gait that is closer to natural [11, 20]. Moreover, the brace incorporates 10 adjustment points.

3.8   Actuation Cart

The actuation cart (Figure 3.7) has four swivel locking wheels that allow mobility to follow the exoskeleton wearer. The outer dimension of the cart is 28" (width) x 18" (length) x 45.84" (height) which was influenced by the dimensions of the housed electronic instrumentation. The frame is made from 80/20 Inc. 1010 T-slotted profile aluminum bars that allow for high adjustability of mounted electronics parts and motors. Although the bars had various lengths to compose the cart, they all had a cross section dimension of 1" height and 1" width. The cart is designed without cover panels on the sides to enable ease of access to hardware and wiring to simplify system troubleshooting. A 1/4 inch thick PVC panel is placed on the top to act as a table.

Figure 3.6: Completed Ankle Exoskeleton

The cart is divided into two main parts: electronic section and mechanical section. These two sections are physically divided by vertical columns that span the height of the cart. The columns were placed to grant independent mounting positions between the motors and electronic parts. Moreover, the column is located 10.5" from the front of the mechanical side, which allocates 9" and 6" of horizontal movement for the mechanical and electrical side, respectively. The mechanical section had a larger space in order to leave the possibility to create larger size motor pulleys for greater torque. The position of the column was dictated by the largest width part which was a desktop PC. Space was incorporated to the base level of the cart to allow the placement of 45lb olympic plates to prevent possible tipping of the actuation cart due to the tension in the Bowden cables. There are three parallel horizontal bars that connect to the bottom layer and have attached perpendicular bars to guide and center the alignment of stacked weighted 45lbs olympic plates. A horizontal handle bar is placed on the electronic side for ease of mobility. See Appendix A for SOLIDWORKS drawings of the actuation cart and Exoskeleton braces.

3.8.1   Mechanical Section

The mechanical section involves the motor assembly (Figure 3.8) which is comprised of an EC 4-pole brushless motor (305015, Maxon Motor) with a GP42C 74:1 planetary gearhead (203123, Maxon Motor), 500 counts/rev, 3 channel, HEDL 5540 Encoder (110514, Maxon Motor), and LM35 temperature sensor (Texas Instruments). The motor assembly is mounted on a plate by a round panel that surrounds the shaft of the gearhead and through the heatsink enclosing the motor. For stable reinforcement, the motor plate's top and bottom edges are mounted to two parallel horizontal bars. The motor assembly can be repositioned in all

Figure 3.7: Completed Actuation Cart

three translational directions to adjust the positioning of the starting point of the Bowden cable sheath. A Bowden termination block module was used to create a termination point for the Bowden sheath and grant the Bowden cable to exit with a linear path from the motor pulley. This module is planted on an independent adjustable height horizontal bar that is offset from the motor pulley but on the same horizontal plane. The motor pulley attached to the shaft of the gearhead has a diameter of 98mm. The heatsink that encompasses the motor is designed with 16 fins and was fabricated using a 3-axis CNC mill. A hole is placed on the side to provide a clear opening to the motor to collect a case temperature reading via the temperature sensor. The heatsinks give the motors the capabilities to produce high torques safely while minimizing overheating.

3.8.2 Bowden Cable Transmission

Figure 3.9 provides a simplified overview of a single motor to brace Bowden cable transmission. This displays the basic setting of the transmission of torque to the brace. The Bowden sheath and the electrical wiring of the load cell and encoder are routed through a lightweight synthetic fiber (Vectran) wiring sleeve to facilitate the wiring identification. This setup can be reapplied and connected with ease to any of the braces by simply reattaching the Bowden termination block to other braces. A maximum of four motors can be set up in this configuration at a time. A similar setup would be considered for simultaneous bidirectional motion of the hip brace except both Bowden cable sheaths would meet in the same relative proximal end of the hip brace.
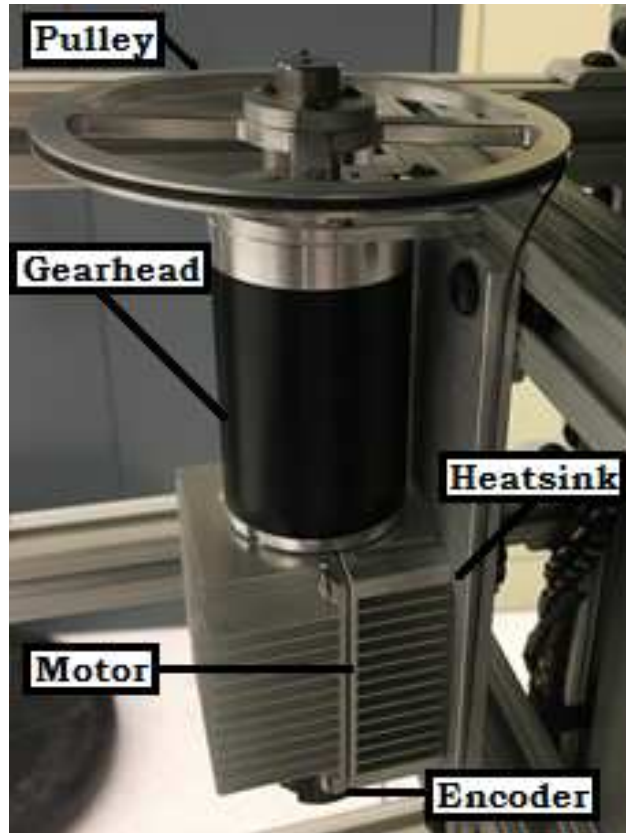
Figure 3.8: Motor Assembly
Order of assembly from the top is a pulley, gearhead, motor, heatsink, and encoder
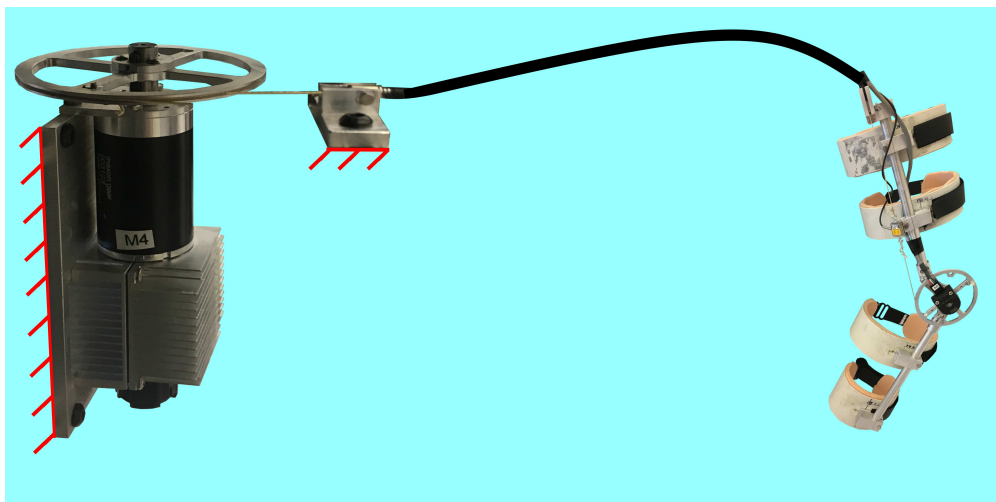

Figure 3.9: Cart-Brace Transmission

3.8.3 Electrical Section

The electronic side contains a DELL OPTIPLEX 760 desktop PC with the additional accessories of a monitor, keyboard, and a mouse occupying the top PVC cover/plate. The computer runs a QNX RTOS 6.5.0 operating system. The desktop acts as a targeted computer in communication to the host computer and has the role of real-time operation of the Quanser Q8 data acquisition (DAQ) board. The Q8 DAQ board has a large range of inputs and outputs: 8 analog inputs, 8 analog outputs, 8 encoder inputs, and 32 digital inputs/outputs. There are three power supplies below the DAQ board attached to a mounting track (DIN rail type) where two are 48V, 10A; 480W power supplies (DRP-480S-48, MEAN WELL USA) and one is a 24V, 3.12A; 75W power supply (DRP-75-24, MEAN WELL USA). The power supplies connect to a 12 outlet 120V surge protector (CPS-1215RMS, CyberPower). The two 48V power supplies connect to four ESCON 50/5 4-quadrant PWM motor amplifiers (409510, Maxon Motor), and the 24V power supply provides power to four force sensor amplifiers (IAA100, FUTEK). Furthermore, the force sensor amplifiers are attached via DIN rails and are placed on the lower side of the mechanical section to distance the device from the power supplies to limit signal interference. Figure 3.10 presents a block diagram of the electrical components of the exoskeleton emulator.

3.9 Brace Characterization and Control System

The exoskeleton control system implements a position feedback Proportional-Integral-Derivative (PID) controller to control the torques applied at the brace joints.
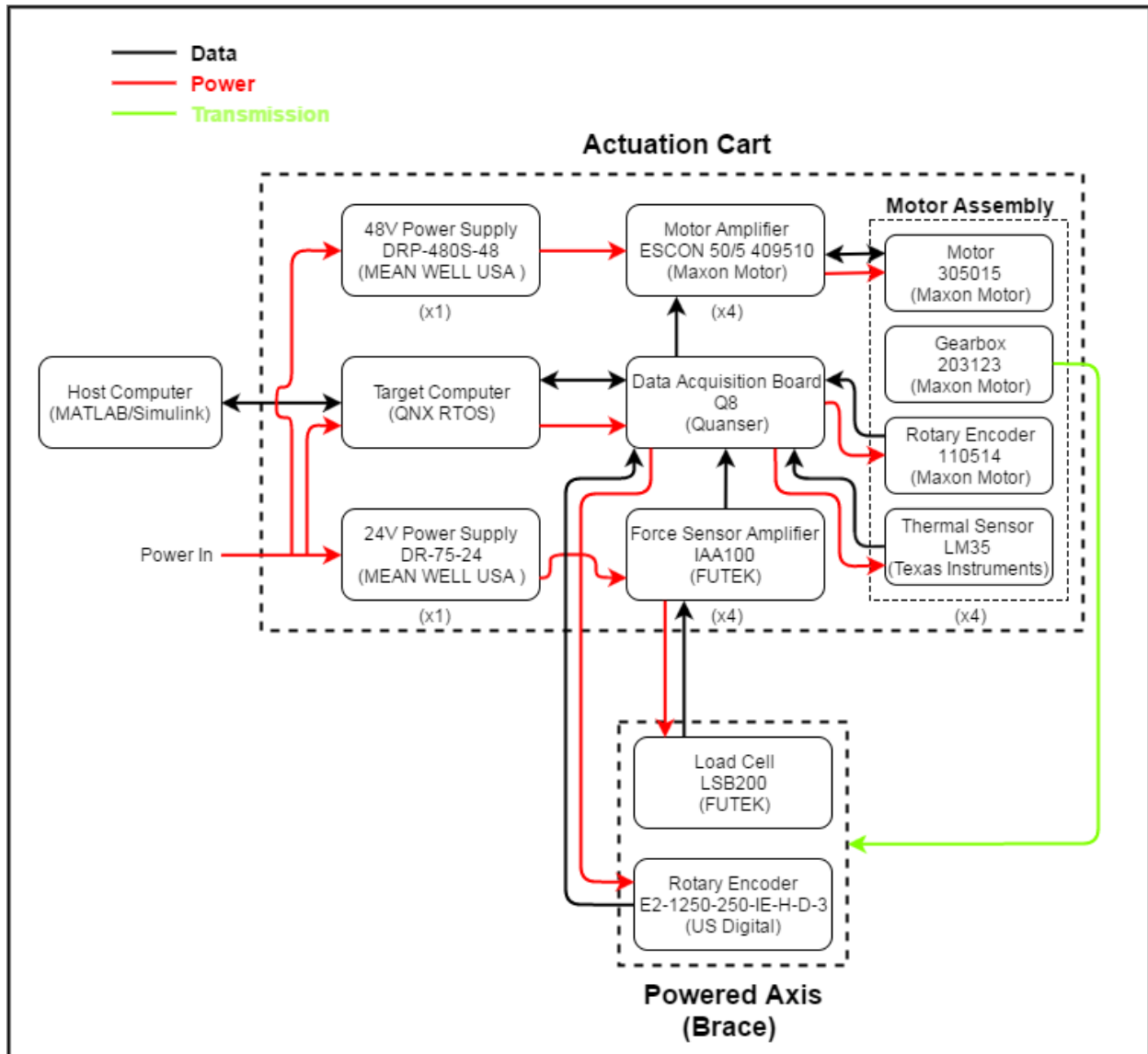
Figure 3.10: Block Diagram of Electrical Components
Block diagram of exoskeleton emulator electrical components and flow of data and power.

The position feedback controller utilizes a least-squares second order regression model to output desired motor position as a function of brace joint angle and desired torque as shown in Equation 3.1.

$$\theta_m = A\theta_b + B\tau_{des}^2 + C\tau_{des} + D \qquad (3.1)$$

θ_m is the desired motor position measured in encoder counts, while θ_b is the current brace position, and τ_{des} is the desired torque at the brace. The braces were first characterized through quasi-static trials that involve rotating the braces' active joints through the full range of motion over a range of continuous force generation (from 2N to 45N). The continuous force is limited by the maximum current output of the motor amplifiers. This process was completed for flexion and extension of the targeted brace to involve the friction forces dependent on the direction from the Bowden sheath in the model. The quasi-static trial would provide the inputs τ_{des}, θ_b, and the polynomial coefficients A, B, and C to obtain the surface plot in Figure 3.11. In order to obtain the desired motor position (θ_m), the braces would require calibration before an experiment to output the polynomial coefficient D. The calibration process would involve conducting the same quasi-static trials as the characterization process, except the range of force would vary from 2N to 15N (which would not require as much time and effort as the characterization process).

Figure 3.12 shows the position feedback PID controller diagram. Where $\theta_{m,des}$ is the desired motor position, $\theta_{m,act}$ represents the actual motor position, e(t) is the error term in respect to time, I_m is the motor current, and τ_{act} is the actual torque. The K_P, K_I, and K_D are the PID gain terms. Once the characterization and calibration process are completed, the desired motor position is input into the position feedback controller. The PID gain terms were tuned and predetermined for the model. The combined PID gains multiplied by the PID error terms output the motor current to the cart's motor which in turn applies the actual torque to the braces. The motor encoder provides the actual motor position controller feedback.
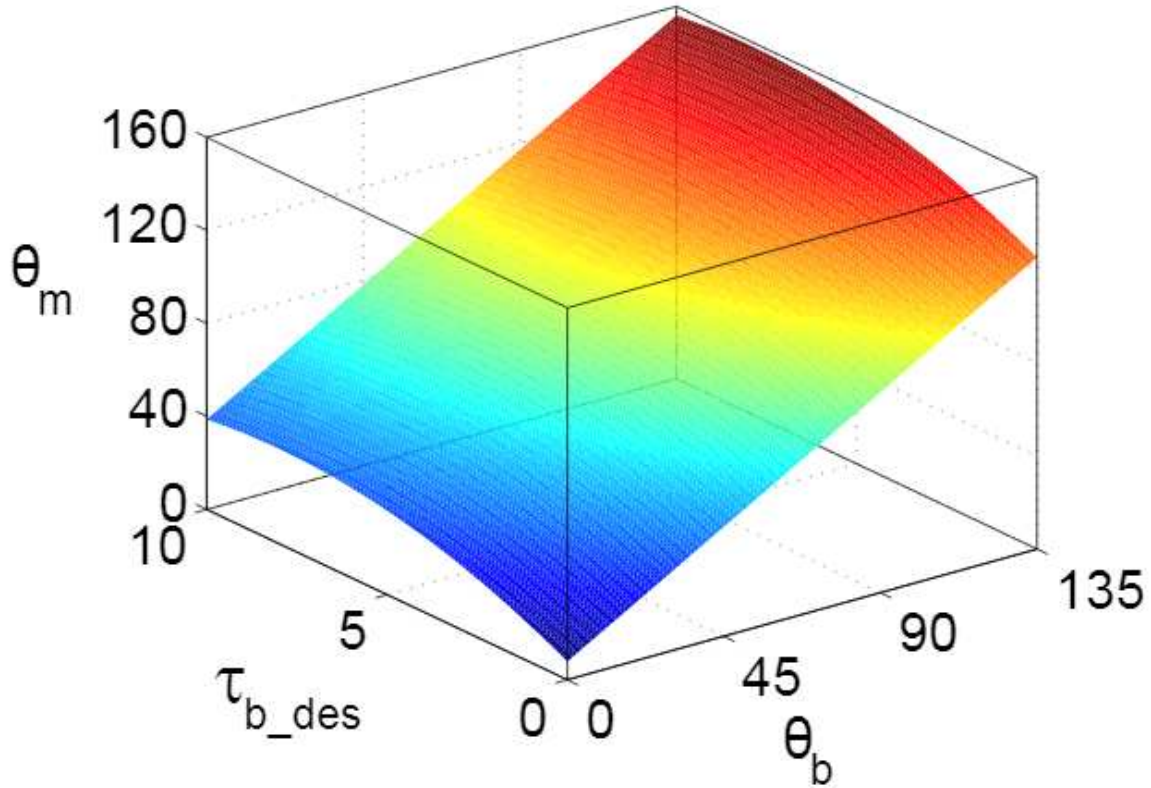
Figure 3.11: Characterization and Calibration Plot
Surface characterization and calibration plot that maps desired motor position in respect to the desired torque and the brace position.

A walking trial at 1.2 m/s was completed using a knee brace in order to gauge the performance of the controller. A transparency mode was developed to allow the user to walk in a brace without any torque being applied while allowing the motor to let in and out cable to control a constant tension. During the trial, both brace and motor encoder counts and load cell readings were measured and modified to output torque. In Figure 3.13, the controller performance is shown with three gait cycles. The torques stay below 0.1 Nm and the motor position follows closely the brace position.
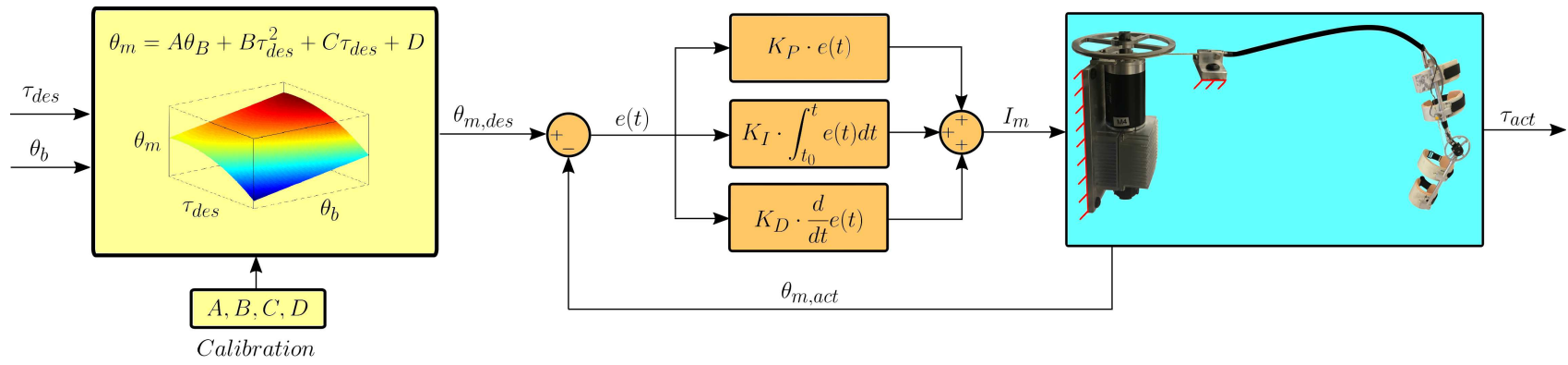
Figure 3.12: Position feedback PID controller
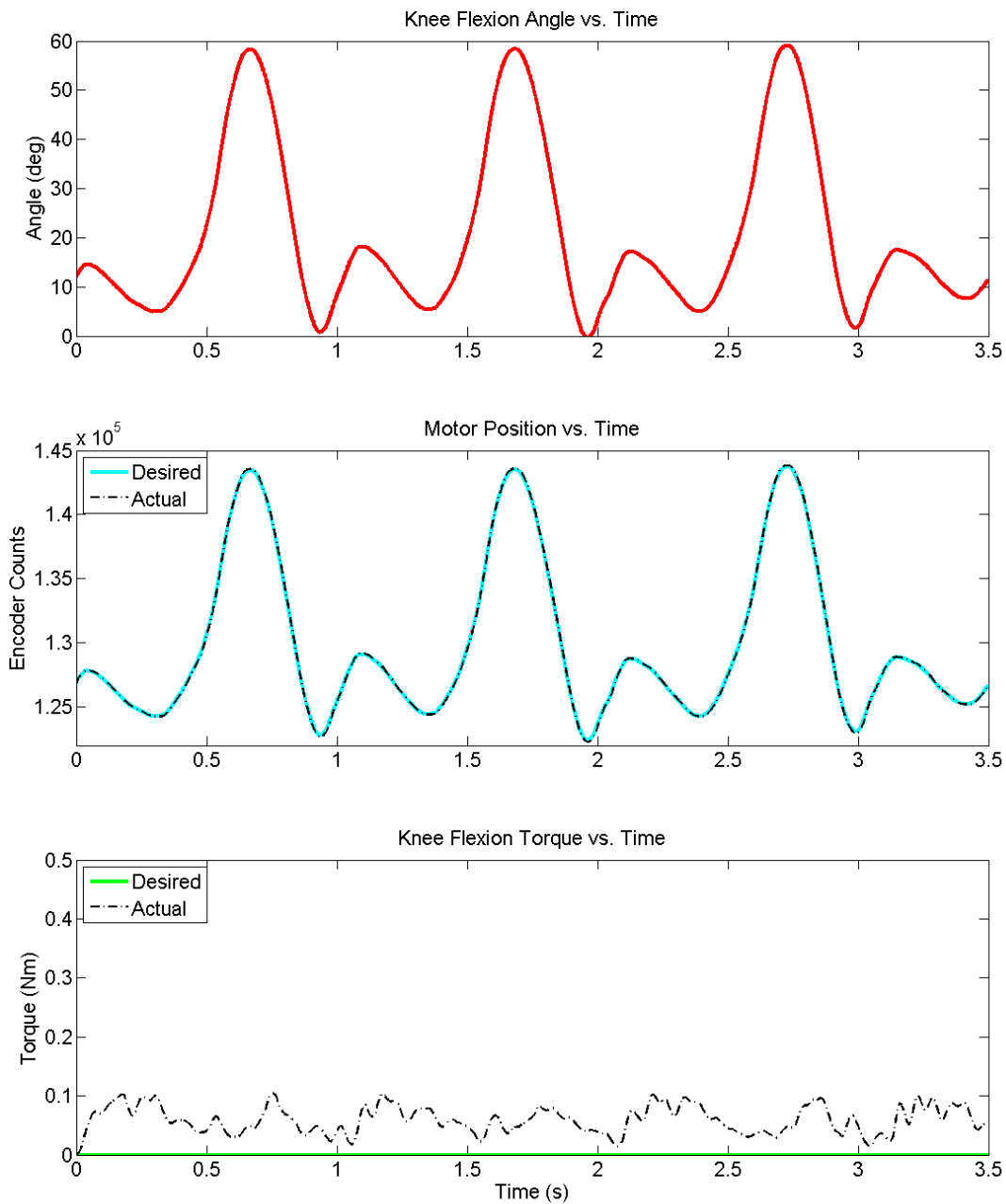
Figure 3.13: Controller Performance Plot

Knee flexion angle, desired vs. actual motor position, and desired vs. actual joint torque during gait at 1.2 m/s with knee brace in transparent mode.

CHAPTER 4

PILOT TESTING

A pilot experiment was used to evaluate and analyze the performance of the actuation

cart and hip brace exoskeleton in a hip joint impedance identification scenario. This section

presents the overview of the experimental protocol, results, and discussion of the completed

pilot experiment.

4.1   Experimental Protocol

The test subject was a healthy, able-bodied individual with no history of lower extremity

injuries. The subject gave verbal consent to participate in the experiment. The experiment

was conducted on a treadmill at a walking speed of 0.8m/s. Also, this speed was chosen

to be less than the standard walking treadmill speed in order to safely test the mechanical

durability of the hip exoskeleton brace against high torques [11].

4.1.1   Control Software

Simulink and MATLAB software packages were used to develop a control model for the

experiment. During the pilot testing, the control system applies torque perturbations at cer-

tain times during gait. The experimental technique of applying a perturbation was modeled

after an ankle impedance identification study [1]. Each perturbation was composed of 75ms

duration and a constant desired torque level of 9.26Nm (or 50lbf in tension). Heel strike

was determined by using the brace encoder data. It was discovered during pre-experiment

walking trials that the hip angular data contains a small but noticeable change in angle

where the anticipated heel strike would occur for a gait cycle as seen in the red circles of Figure 4.1. Upon further observation, it was revealed during heel strike that the interactive force from the treadmill to the sole causes a natural perturbation that ultimately effects the hip joint angle. Taking full advantage of this dip in angular position, a close approximation of the identification of heel strike can be determined. The first step to determine the time of heel strike in the control model was to find the maximum peaks of the hip angle. Secondly, the control model would actively pinpoint the next local minimum value (dip) of the brace angular velocity. This value corresponded to the timing of the heel strike. The hip angle surrounding the timing of heel strike was not a reliable condition to identify heel strike because of the applied perturbations' potential effect on the position. The angular velocity contained a local minimum peak that was caused from treadmill impact but displayed consistent peaks that were independent of the small dip in hip angle. Figure 4.1 exhibits the control model process for determining the activation of heel strike during walking.

After heel strike occurs, a perturbation can be applied at 2.5%, 12.5%, 22.5%, 32.5%, 42.5%, 52.5%, 62.5%, 72.5%, 82.5%, and 92.5% of the gait cycle for a total of 10 perturbation timings (Figure 4.2). These timings are selected in order to obtain information for the full gait cycle. The perturbation timings are percentages to allow ease of comparison for different speeds and for various timings of subjects' individual gait cycles. Additionally, the total time of the gait cycle varies with human speed where walking at 1.2m/s may on average take approximately 1s while running at 3.2m/s could take 0.7s [11].

Since the model runs in real time and the individual, full gait cycles times were different, an average estimated stride time (EST) was calculated to estimate the perturbation timing in real time. EST was defined as the time needed to complete a full gait cycle from heel
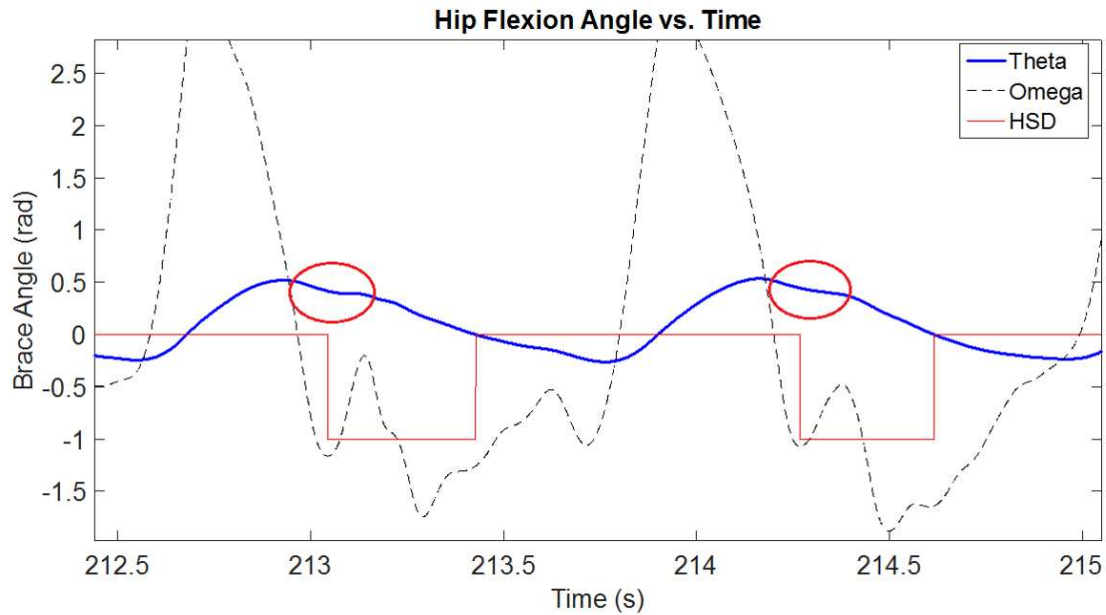
Figure 4.1: Experimental Hip Joint Angle
Theta - hip angular position, Omega - Angular velocity of the hip brace, HSD - Heel Strike
Determined. The red circles represent the slight abnormal change in angle that is caused by
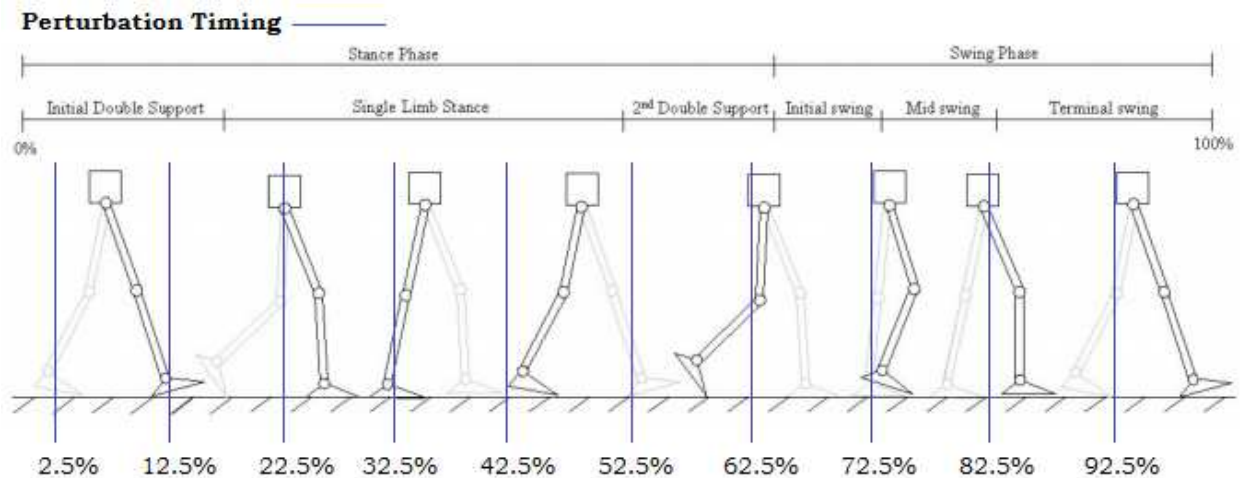heel strike on the treadmill.

Figure 4.2: Perturbation Timing Percentages
Perturbation timing percentages for the full gait cycle. The vertical bars represent the time
of the perturbation for an individual gait cycle.

strike to heel strike. A 2-minute walking trial at 0.8m/s was conducted to determine each

gait cycle's EST using the right leg. The EST was averaged and was utilized as an input to

35

the control model for the perturbation experiment. During real time, the randomly selected perturbation timing percentage would be multiplied by the EST value which would lead to the timing of the perturbation. Two motors were used for this experiment in order to implement perturbations in bi-directional (hip flexion/extension) motion of the right hip. Figure 4.3 exhibits the experimental setup of the two motors where the Bowden cables were routed towards the midway point between both pulleys. Individually, the motors apply torque in one direction of either flexion or extension while the other motor releases the cable to make it slack.

There were a total of 60 perturbations that were applied with 30 representing flexion and the rest representing extension. A total of six perturbations would occur at each perturbation timing point. Having a controlled number of perturbations grant an even distribution of perturbation occurrences for each timing point. The control model was set up to have the perturbation timings occur randomly to prevent the subject from anticipating a perturbation. A random number generator was created to contain 60 numbers that range from integers of 1 to 10. Each number would occur randomly in a vector six times with three of the six numbers being negative to tell the control model whether the perturbation will be applied in flexion or extension direction. Only a single perturbation was applied during one gait cycle. When the trials begin, the perturbations occur at random at any stride, but once a perturbation occurs another perturbation was not activated until after at least three strides. After the three strides were completed from the initial perturbation, then the perturbation can occur at a random stride before the eleventh stride. This allows the user to not anticipate when perturbations would appear as well as ensuring the subject can have time to restore normal gait kinematics after a perturbation.
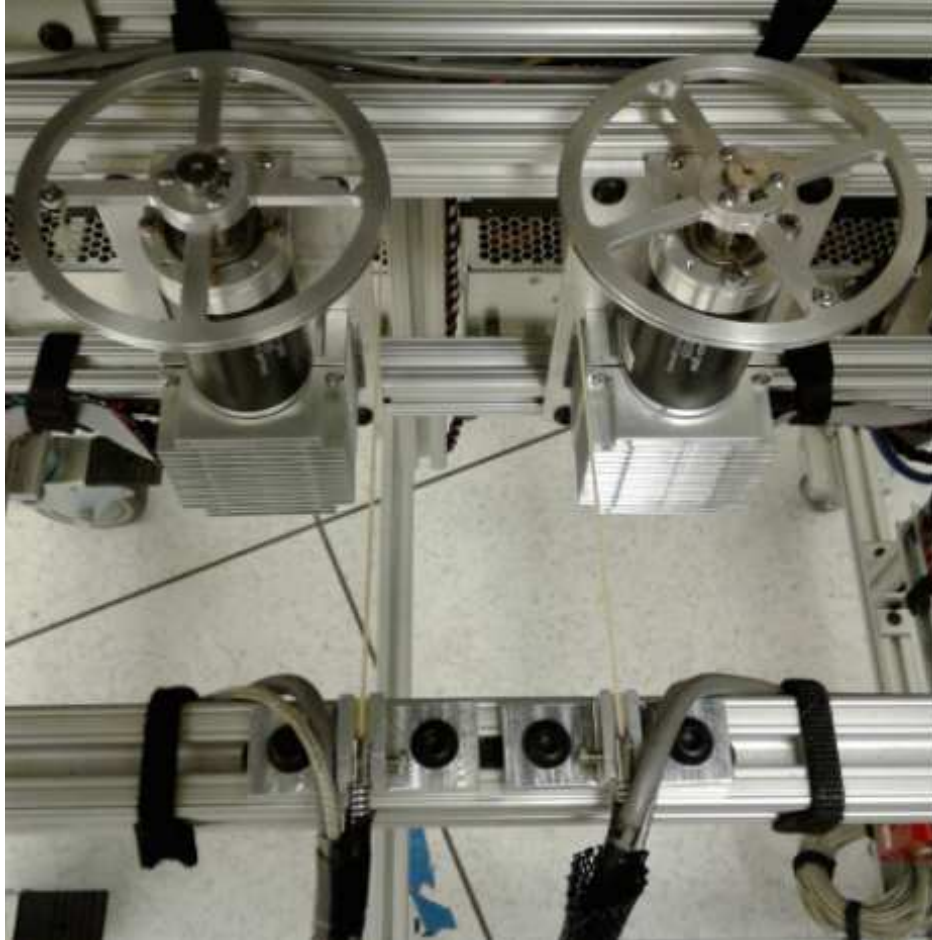
Figure 4.3: Experimental Motor Setup
The motors rotate in the same direction during the active motion of the hip brace. The Bowden cables are routed in the above orientation to grant both motors to rotate in the same direction during active motion of the hip brace.

4.1.2 Safety Measures

There are several safety measures in effect to prevent injury to the wearer. First, there are mechanical hard stops on the hip exoskeleton to prevent injury of overextending the hip joint. Secondly, for emergency purposes, an emergency stop switch was installed on the actuation cart that will remove power from the motors. For future experiments, a body harness will be installed in the lab that would be hunged from a zip line, allowing linear mobility that spans the full length of the lab. The zip line would be rated to carry loads up

to 300lbs.

4.1.3 Human-Brace Alignment

The hip exoskeleton was placed on the subject by first attaching the lower torso cuffs, and then strapping the thigh cuffs in. A single experimenter adjusted the alignment of the hip exoskeleton to ensure that the device was securely and comfortably attached to the user. Once the cuff attachments were securely tightened, the experimenter adjusted the segment rods of the brace until the passive and active joints were centered around the anatomical joints. During this process, the experimenter got constant verbal feedback from the wearer in terms of compatibility and mobility point of view. The wearer would be asked to extend their leg and rotate it in a circular motion. This exercise helped the experimenter identify the location of the hip center of rotation. Furthermore, physical contact with the pelvis and femur served as additional feedback and gave the experimenter general reference points of the hip joint. The adjustment and alignment of the exoskeleton's hip joint center to the human was a lengthy process. The total time to complete the adjustments was approximately 30 minutes. Figure 4.4 displays a close up sagittal view of the hip exoskeleton alignment with the wearer's hip joint during the experiment. Moreover, the image exhibits the simultaneous bi-directional Bowden cable setup where there were two force sensors that were attached separately but in series with the Bowden cable and overlapped around the pulley.
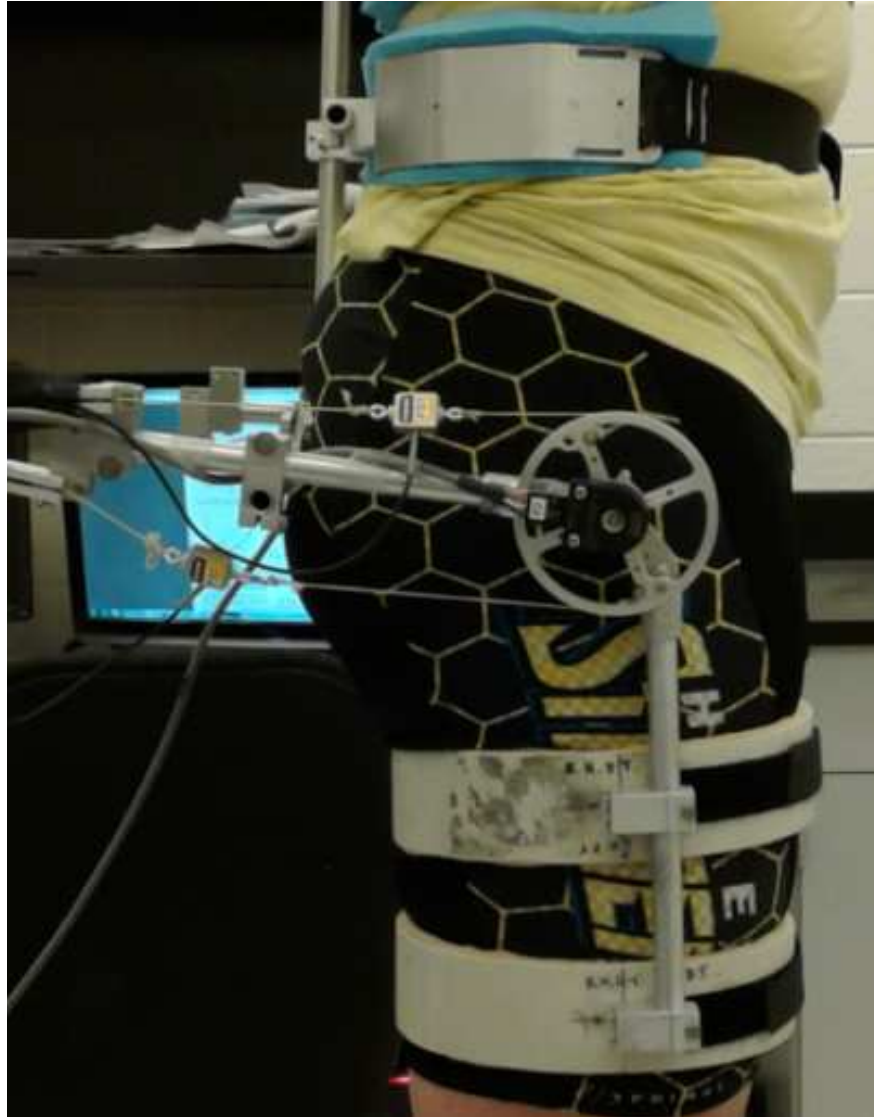
Figure 4.4: Hip Brace Alignment
Hip brace final alignment for pilot testing in the sagittal view. Note the bi-directional cable attachment setup.

4.1.4 Experimental Method

The general setup of the experiment and placement of the devices is shown in Figure 4.5. See Appendix B to view additional photos of the experimental setup. The Bowden sheaths were hung by cables in order to reduce curvature of the cables and thus limit the friction. Each time before the subject was going to walk on the treadmill, a standing static

measurement of the hip angle was taken to obtain a baseline for angular position. 2 minutes and 30 seconds was allocated to subjects walking on the treadmill at a speed of 0.8m/s with the hip brace without perturbations being applied for warm up and familiarization with the device. The first 30 seconds were devoted for subject to obtain a natural gait. Brace encoder values were recorded in order to calculate the EST values. In order to minimize the effect of fatigue on the data, the subject was given as much time and rest as he needed between the trials to recuperate. The second part of the experiment involved the subject walking with the hip brace being active with perturbations being applied. There was no set time limit on the perturbation trial since the subject needed to endure 60 total perturbations. The time to complete the perturbation trial was approximately 15 minutes. Again, the first 30 seconds are without any perturbations so that the subject will begin in a natural walking pattern.

4.2   Data Analysis

MATLAB was used to analyze the data. Overall, the goal was to collect hip joint angle response and applied torque during the perturbation trials and obtain the angle profiles of the non-perturbed trials using the sensors of the hip brace. These data were used to determine the impedance of the hip joint. In order to collect the joint angle and torque, the force applied was first observed to determine the time that the perturbation occurs. It is shown in Figure 4.6 that the actual force measured was delayed from the desired force by approximately 30ms. Moreover, the actual force varies in magnitude for different perturbations.
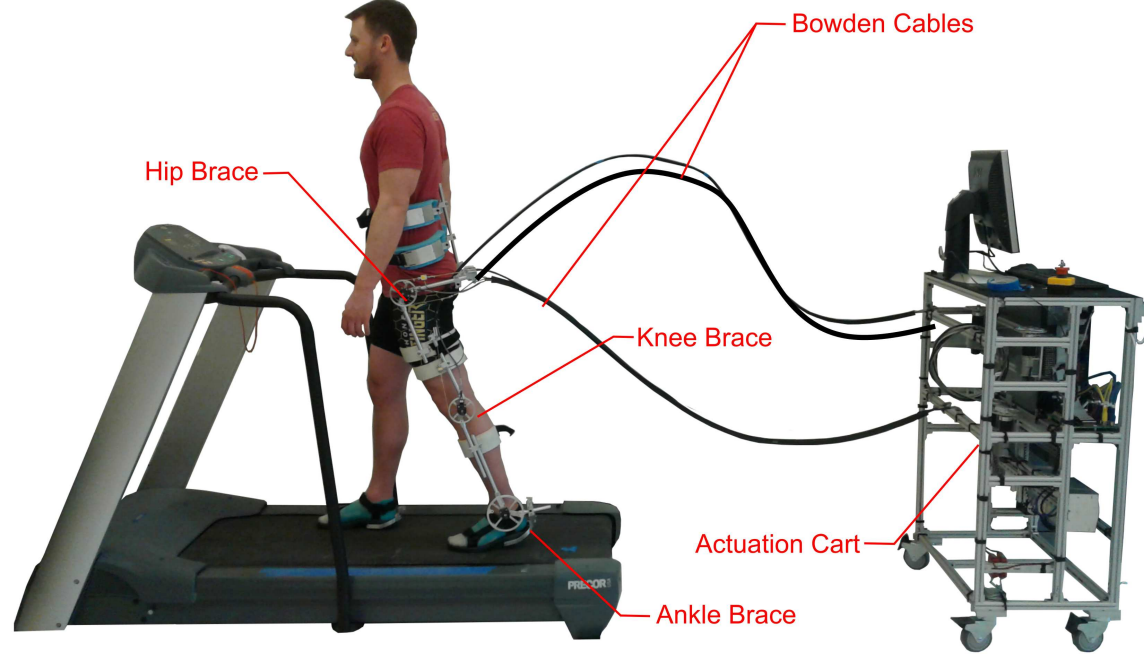
Figure 4.5: Exoskeleton Emulator System Experimental Setup

Body harness is not shown. The actuation cart is placed directly behind for a linear path of the Bowden cables. There are four Bowden cables drawn to the hip exoskeleton. The experiment does not use the knee and ankle brace shown. The Bowden cable sheath also carries the electrical wiring of the encoder and force sensor wrapped around using heli-tube.

The start of the perturbation timing is critical for identifying the individual perturbed angle within the specific timing window. To spot the time of the beginning of the actual perturbation, the peaks from the force cell readings were located and 100ms was subtracted. Another method for identifying the start of the perturbation was developed by setting a threshold of 0.75lbf and searching the time instances when the force profile would be greater than the threshold. Both methods were computed and compared by averaging the difference between the values for each perturbation. The average difference was 4ms and 7ms for flexion and extension perturbations, respectively. Since the differences between these two results were negligible, obtaining the peak method was utilized.
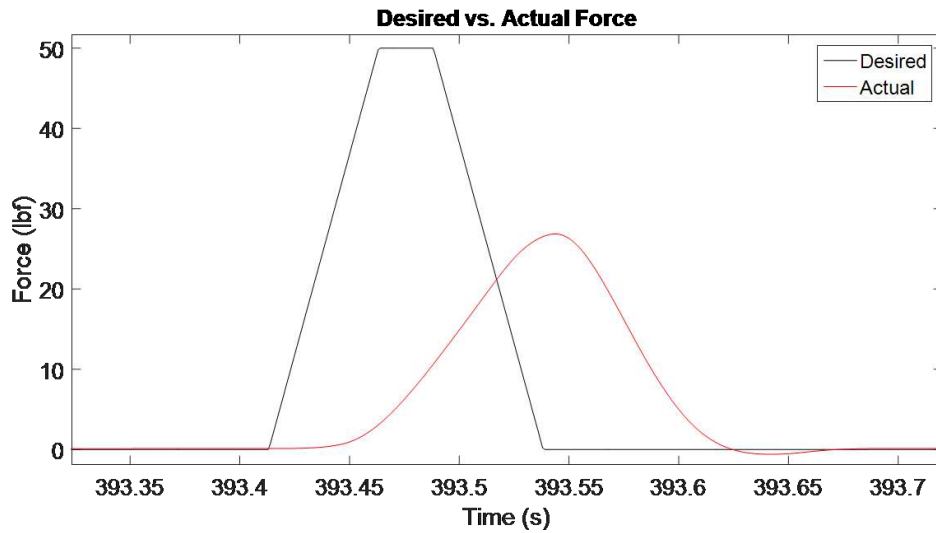
Figure 4.6: Actual and Desired Torque Profiles
The actual force is delayed from the desired force applied by approximately 30ms.

Once all start times of the perturbations were collected, all heel strike times that occur right before the perturbation were obtained. The difference was calculated and divided by the average EST to equate to the actual perturbation percentage timing. These values were sorted for each perturbation time and direction and averaged, results of which are displayed

in Table 4.1.

Table 4.1: Desired and Actual Average Perturbation Timing Percentages

Desired	Actual	
Timing %	Flexion	Extension
2.5%	5.5%	4.8%
12.5%	15.1%	14.9%
22.5%	25.3%	24.9%
32.5%	35.5%	35.0%
42.5%	45.7%	44.9%
52.5%	54.9%	54.9%
62.5%	65.2%	64.0%
72.5%	75.5%	74.1%
82.5%	85.7%	84.3%
92.5%	95.4%	95.1%

The average unperturbed angle profiles were output by collecting a 75ms data window that began at the calculated average perturbation timing percentages. This timing was solved by multiplying the average perturbed timing percentages by the average EST and adding to the previous heel strike time. These data were gathered from the first unperturbed walking trial and the angle profile was averaged for each gait cycle across each perturbation timing. The average perturbed angle was obtained from the perturbation trial and a 75ms data sets were gathered that started at each of the previously estimated perturbation timing percentages. These data set were averaged between each perturbation timing. Figure 4.7 and Figure 4.8 compare the average unperturbed and perturbed angles for a full gait cycle and displays a close up view.

The perturbed angle profiles were offset to allow both angle profiles to start at the same position. To isolate the perturbed angle profiles from the unperturbed values, the
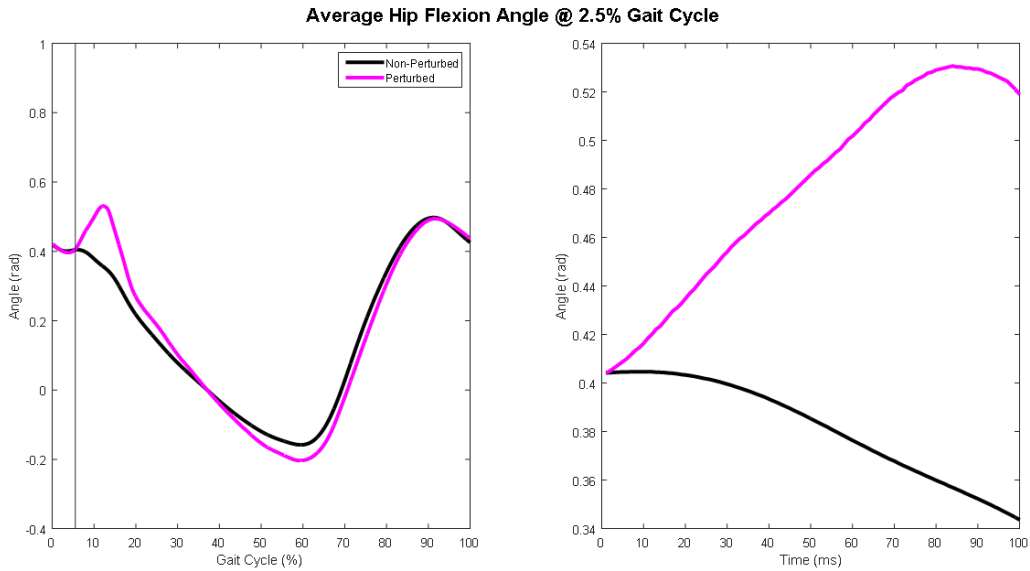
Figure 4.7: Average Hip Angle (Flexion Perturbations)
(Left) Plot of full gait cycle. The vertical gray line (at 2.5%) serves as a landmark to the occurrence of the perturbation. Perturbation occurs at a desired 2.5% of the gait cycle. (Right) 100ms window plot of the start of the perturbation.
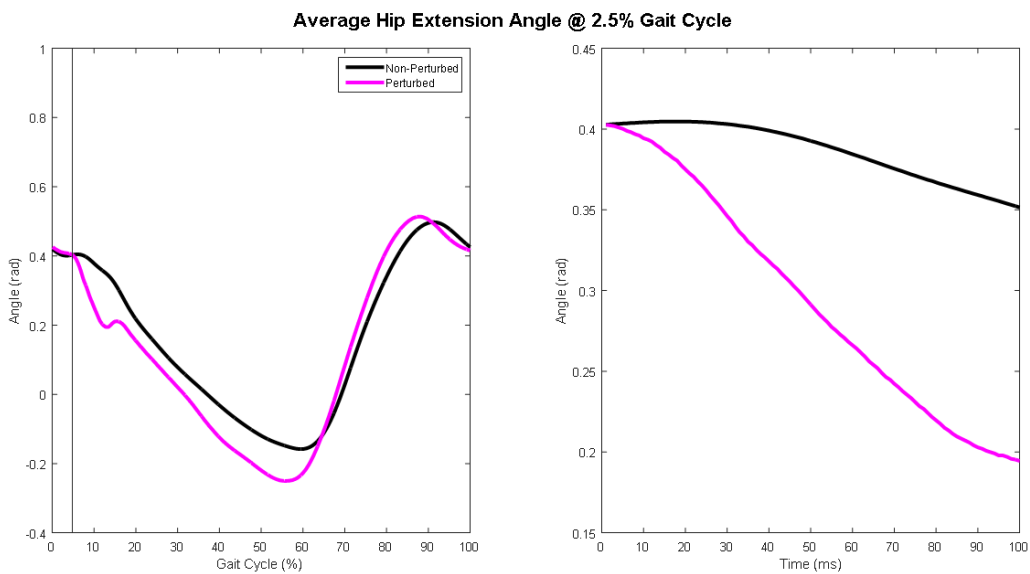

Figure 4.8: Average Hip Angle (Extension Perturbations)
(Left) Plot of full gait cycle. The vertical gray line (at 2.5%) serves as a landmark to the occurrence of the perturbation. Perturbation occurs at a desired 2.5% of the gait cycle. (Right) 100ms window plot of the start of the perturbation.

44

average perturbed angle was subtracted from the average unperturbed angle profiles. This subtraction would result in a resultant angle that had any offset eliminated so that the profiles begin at zero (Figure 4.9). The force measured from the load cell was converted to torque. The force measurements related to hip flexion were set to negative values in order to set the rotational directions of the torque. The torque profile also contains a 75ms data set that was based off the beginning of the perturbation and was ultimately averaged for each perturbation timing.
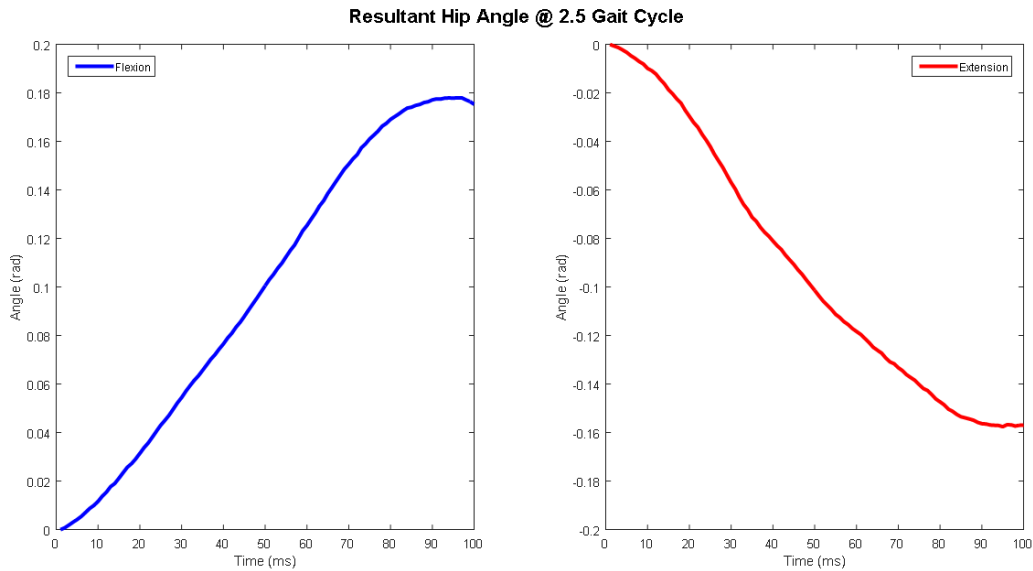
Figure 4.9: Resultant Hip Angle

This technique to estimate impedance has been validated by two identification studies of an ankle-foot prosthesis and the stiffness of an ankle joint during stance phase [3]. The resultant angle and torque profile would be input to a second-order parametric model to characterize the impedance of the hip joint as shown in Equation 4.1.

$$\tau_p = I_t \ddot{\theta}_r + b_h \dot{\theta}_r + k_h \theta_r \tag{4.1}$$

In this equation, θ_r represents the resultant hip joint angle profile. τ_p was the torque applied during the perturbation trials. I_t was the total inertia of the hip and surrounding body portions. The damping and stiffness coefficients of hip impedance were respectively expressed as b_h and k_h. A second-order polynomial fit of 5 points encompassing each millisecond of the resultant angle profile was used to derive the resultant angle to solve for angular velocity and acceleration [42]. There have been previous studies showing that selecting a second-order polynomial has given satisfactory calculations of joint impedance [4, 5, 43, 44]. The MATLAB command *polyfit*, *polyder* and *polyval* are used to create a second order polynomial's coefficients, take the derivative of those coefficients, and evaluate them at each time point. A 2nd order Butterworth low pass filter was applied to the velocity and acceleration profiles with a time sampling rate of 1ms. The filter had a cutoff frequency of 15Hz and 10Hz for the velocity and acceleration, respectively. The hip dynamic (resultant angle, velocity, and acceleration) profiles are shown in Figure 4.10. A least squares estimation was used to calculate hip impedance [45]. The MATLAB command *lsqlin* was utilized to solve for impedance with lower bound constraints implemented. The lower constraints are set to zero since it is unreasonable for the impedance values to be negative. Ultimately, several plots are generated connecting the inertia, damping, and stiffness values at each timing point throughout the gait cycle for walking. To validate the results of the impedance values, the impedance values were input into Equation 4.1 to output a calculated torque. The calculated torque and the experimental torque are compared in Figure 4.11. Appendix C contains additional plots for all perturbation timings for Figures 4.7-4.11.
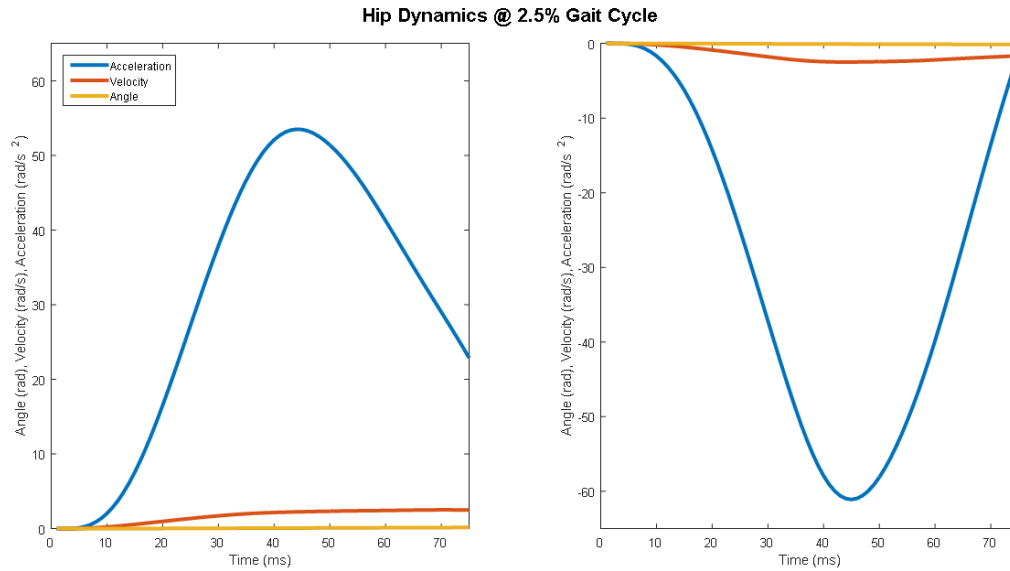
Figure 4.10: Hip Dynamic Profiles
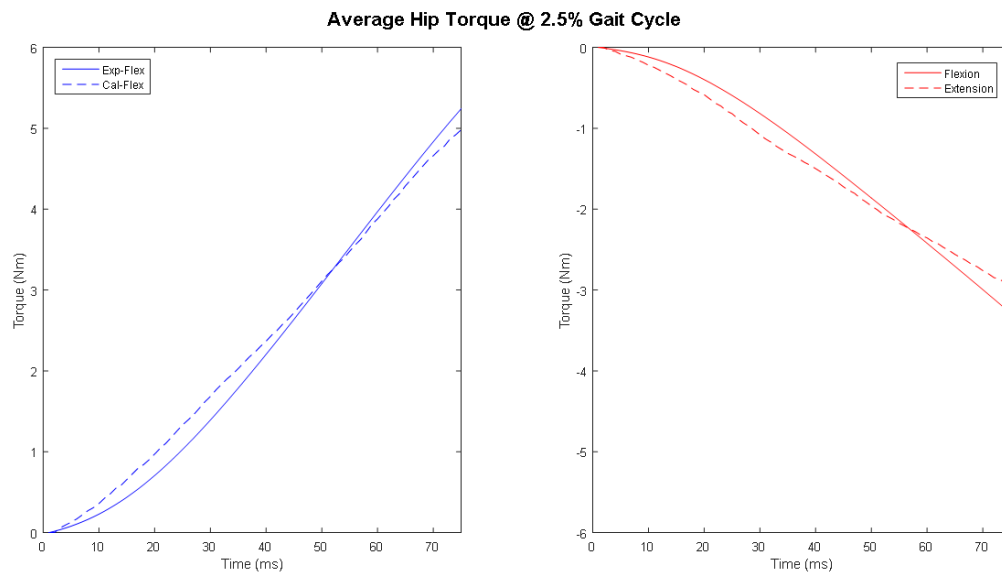Resultant hip angle, angular velocity, and angular acceleration

Figure 4.11: Average Hip Torque

4.3 Results

Figure 4.12 presents the stiffness, damping, and inertia calculated at each perturbation

timing percent. Observing the stiffness values, the extension values increase linearly from

20.26Nm/rad to 36.43Nm/rad during the stance phase. Then the values decrease and eventually level off around 20Nm/rad. The flexion values follow a similar trajectory where there was a general rising linear trend starting from 30.94Nm/rad and peaks to 39.69Nm/rad. The trend was increasing but was sporadic with values decreasing slightly before rising greatly. A large drop off of stiffness values occur during swing phase where the last four values range from 20.89Nm/rad to 24.81Nm/rad. At 62.5% of the gait cycle, there was an abnormal extension stiffness value since it is near zero.
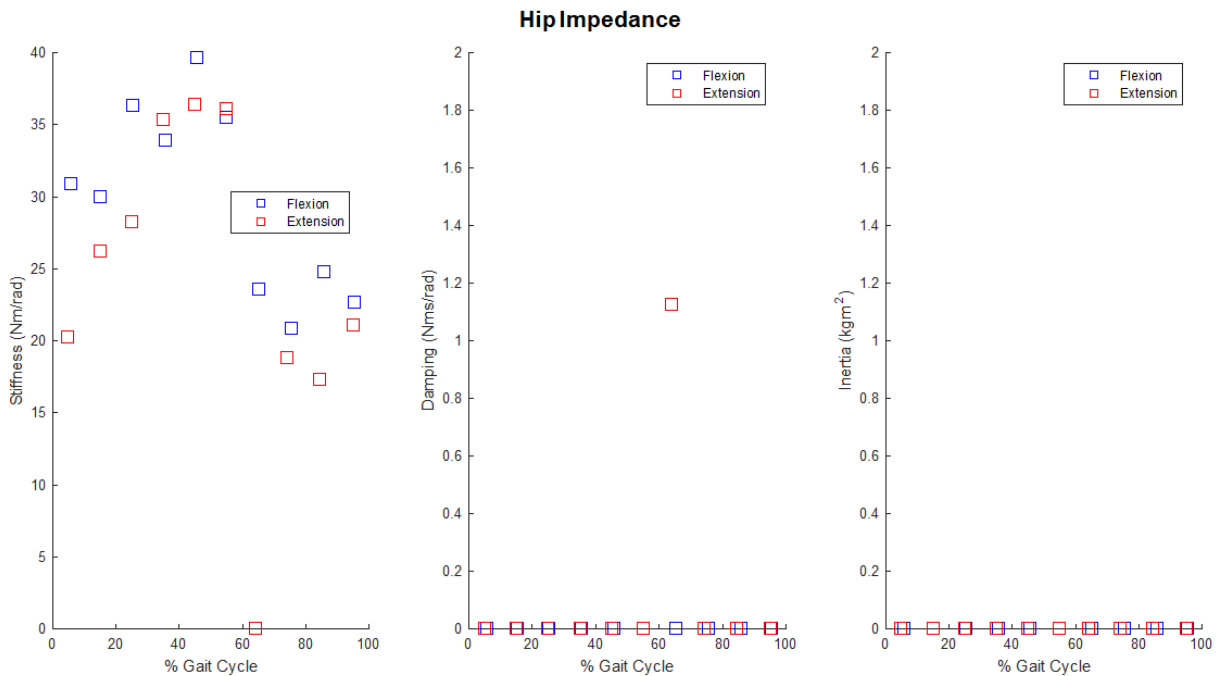
Figure 4.12: Hip Impedance Values

All of the hip damping values besides one extension value were practically zero. The one value not near zero occurs at 62.5% of the gait cycle and has an impedance value of 1.128Nms/rad. The inertia values were similar to the damping values where all values are practically zero.

4.4 Discussion

An exoskeleton emulator for the lower-limb was successfully designed, constructed, characterized, and tested. The exoskeleton emulator will enable a variety of future studies on gait augmentation and assistance. A pilot test was conducted to determine the identification of joint hip impedance for a single person at a walking speed of 0.8m/s.

4.4.1 Impedance Estimation and Limitations

Overall, the flexion/extension stiffness values follow the trajectory of an inverted parabola where the values increase during the stance phase and decrease during the swing phase. In general, the curves present a similar trend comparable to the hip quasi-stiffness in Figure 2.2. It would be implied that since the ankle stiffness values closely aligned with the quasi-stiffness, the hip stiffness would be congruent to the hip quasi-stiffness [31]. Both the stiffness plot and the quasi-stiffness plot begin at an initial value, peaks during pre-swing, and returns to the approximal initial value. Intuitively, the stiffness gradually increases and peaks from heel strike to pre-swing because more stability and balance were required building up to the toe-off event. Also, this progression increases since the body's center of mass was moving forward over a single leg. Moreover, the stiffness values during the swing phase would be relatively lower since the leg does not need to support the body.

The obtained damping and inertia values were unexpected and all were close to zero. Several factors play into this result; however, the primary reasons have been determined as insufficient perturbation amplitudes and significant losses in transmission of these torques to the leg. The applied torques mainly end up compressing the soft tissue at the cuff attachment points, hence moving the exoskeleton with respect to the person, rather than

49

moving the person's leg with itself. Proper identification of the inertia and damping values require larger torque perturbations and a more effective transmission of these torques to the wearer. The highest absolute average torque applied for all perturbation timings was 5.56Nm (0.06Nm/kg) and 4.34Nm (0.05Nm/kg) for flexion and extension, respectively. A study that measured hip torques for walking over a treadmill reported a range of approximately 0.5Nm/kg to -0.5Nm/kg [46]. The torques applied to the hip in the pilot test were a magnitude smaller than these reported hip torques, which may not sufficiently perturb the leg. The torque required to achieve a greater perturbation may need to be equal or greater than the measured hip torque in order to lead to proper impedance estimations.

Another possibility for low impedance values was that the impact from the perturbation torque may be absorbed by the surrounding body and soft tissue. Additionally, the attachment cuffs strap around the thigh and lower torso which contain the most soft tissue in the legs. Even though the attachment points were secured tightly on the subject, some perturbations forced the attachment cuffs to flex independent of the body. This led to the hip brace joint bending more than the subject's hip joint. Therefore, there is loss of energy in the torque applied.

There were two additional limitations to the study. First, the data in the study was limited due to having only a single subject. Second, there was room for error in the alignment of the brace with the hip center of rotation due to the visual inspection of the location of the center of rotation.

4.5 Future Work

The attachment cuffs of the exoskeleton could be improved upon to be more secure and to more effectively transmit torques between the exoskeleton and the wearer. There are several factors that can enhance the applied torque at the brace. Firstly, the control system had a limit for the motor current at 5A, but the maximum intermittent current allowed at the motor amplifiers was 15A, which can allow generation of higher torques particularly in perturbation studies. Secondly, the brace pulley radius can be expanded and the motor pulley radius can be reduced to further amplify torque. Lastly, the motor gearhead ratio can be increased. An experimental protocol that was prepared for testing with a larger subject pool is currently in the process of obtaining Colorado Multiple Institutional Review Board (COMIRB, University of Colorado Denver Anschutz medical campus) approval. Ten healthy subjects, five male, and five female participants are planned to be recruited for this study. Impedence data could be collected throughout the full gait cycle for different speeds of walking and running. A statistical analysis could be carried out to evaluate any significant differences in results. Impedence data could be collected throughout the full gait cycle for different speeds of walking and running.

4.6 Conclusion

Overall, a modular lower-limb exoskeleton emulator system with offloaded actuation was developed, integrated, and characterized. After controller implementation was completed, the device was put to use in a pilot test with a single subject that focused on identification of hip impedance values during normal gait. Data obtained from the test revealed that the perturbation amplitudes were insufficient and soft tissues at the leg attachment points

prevented delivery of the torques to the leg. Future work on impedance estimation needs to resolve these limitations.

REFERENCES CITED

[1] E. Rouse, L. Hargrove, E. Perreault, and T. Kuiken. Estimation of human ankle impedance during the stance phase of walking. *IEEE Transactions on Neural Systems and Rehabilitation Engineering*, 22(4):870–878, 2014.

[2] S. Kamran, G. Sawicki, and A. Dollar. Estimation of quasi-stiffness and propulsive work of the human ankle in the stance phase of walking. *PloS One*, 8(3):e59935, 2013.

[3] E. Rouse, L. Hargrove, E. Perreault, M. Peshkin, and T. Kuiken. Development of a mechatronic platform and validation of methods for estimating ankle stiffness during the stance phase of walking. *ASME Transaction on Biomechanical Engineering*, 135(8): 081009, 2013.

[4] R. Kearney and I. Hunter. Dynamics of human ankle stiffness: Variation with displacement amplitude. *Journal of Biomechanics*, 15(10):753–756, 1982.

[5] H. Lee, P. Ho, M. Rastgaar, H. Krebs, and N. Hogan. Multivariable static ankle mechanical impedance with active muscles. *IEEE Transactions on Neural Systems and Rehabilitation Engineering*, 22(1):44–52, 2014.

[6] M. Tucker, A. Moser, O. Lambercy, J. Sulzer, and R. Gassert. Design of a wearable perturbator for human knee impedance estimation during gait. *Rehabilitation robotics (ICORR), 2013 IEEE international conference on. IEEE*, pages 1–6, 2013.

[7] S. Kamran, G. Sawicki, and A. Dollar. Estimation of quasi-stiffness of the human knee in the stance phase of walking. *PloS One*, 8(3):e59993, 2013.

[8] K. Shamaei, M. Cenciarini, A. Adams, K. Gregorczyk, J. Schiffman, and A. Dollar. Effects of exoskeletal stiffness in parallel with the knee on the motion of the human body center of mass during walking. *Robotics and Automation (ICRA), 2015 IEEE International Conference*, pages 5557–5564, 2015.

[9] M. Wiggin, G. Sawicki, and S. Collins. An exoskeleton using controlled energy storage and release to aid ankle propulsion. *Rehabilitation Robotics (ICORR)*, pages 1–5, 2011.

[10] S. Collins, M. Wiggin, and G. Sawicki. Reducing the energy cost of human walking using an unpowered exoskeleton. *Nature*, 522(7555):212–215, 2015.

[11] T. Novacheck. The biomechanics of running. *Gait and Posture*, (7):77–95, 1998.

[12] H. Kazerooni. The berkeley lower extremity exoskeleton project. *Experimental Robotics IX. Springer Berlin Heidelberg*, 21:291–301, 2006.

[13] C. Walsh, K. Endo, and H. Herr. A quasi-passive leg exoskeleton for load-carrying augmentation. *International Journal of Humanoid Robot*, 4(3):487–506, 2007.

[14] J. Veneman, R. Kruidhof, E. Hekman, R. Ekkelenkamp, E. Van Asseldonk, and H. Van Der Kooij. Design and evaluation of the lopes exoskeleton robot for inter-active gait rehabilitation. *IEEE Transaction on Neural Systems and Rehabilitation Engineering*, 15(3):379–386, 2007.

[15] H. Kawamoto, T. Hayashi, T. Sakurai, K. Eguchi, and Y. Sankai. Development of single leg version of hal for hemiplegia. *In Engineering in Medicine and Biology Society, 2009. EMBC 2009. Annual International Conference of the IEEE*, pages 5038–5043, 2009.

[16] H. Quintero, R. Farris, and M. Goldfarb. A method for the autonomous control of lower limb exoskeletons for persons with paraplegia. *Journal of Medical Devices*, 6(4):041003, 2012.

[17] C. Buesing, G. Fisch, M. ODonnell, I. Shahidi, L. Thomas, C. K. Mummidisetty, K. J. Williams, H. Takahashi, W. Rymer, and A. Jayaraman. Effects of a wearable ex-oskeleton stride management assist system (sma) on spatiotemporal gait characteristics in individuals after stroke: a randomized controlled trial. *Journal of Neuroengineering and Rehabilitation*, 12(1):69, 2015.

[18] D. Zanotto, P. Stegall, and S. Agrawal. ALEX III: A novel robotic platform for gait training - design of the 4-DOF Leg. *IEEE International Conference on Robotics and Automation*, pages 3914–3919, 2013.

[19] V. Roger, A. Go, D. Lloyd-Jones, E. Benjamin, J. Berry, W. Borden, D. Bravata, S. Dai, E. Ford, C. Fox, et al. Heart disease and stroke statistics–2012 update: A report from the american heart association. *Circulation*, 125(1):e2–e220, 2012.

[20] A. Dollar and H. Herr. Lower extremity exoskeletons and active orthoses: Challenges and state-of-the-art. *IEEE Transactions on Robotics*, 24(1):144–158, 2008.

[21] J. Bae, S. De Rossi, K. ODonnell, K. Hendron, L. Awad, T. Dos Santos, V. De Araujo, Y. Ding, K. Holt, T. Ellis, and C. Walsh. A soft exosuit for patients with stroke: Feasibility study with a mobile off-board actuation unit. *In Rehabilitation Robotics (ICORR), 2015 IEEE International Conference*, pages 131–138, 2015.

[22] Y. Ding, I. Galiana, A. Asbeck, S. Rossi, J. Bae, T. Santos, V. Araujo, S. Lee, K. Holt, and C. Walsh. Biomechanical and physiological evaluation of multi-joint assistance with soft exosuits. *IEEE Transactions on Neural Systems and Rehabilitation Engineering*, 25(2):119–130, 2016.

[23] Y. Ding, I. Galiana, C. Siviy, F. Panizzolo, and C. Walsh. IMU-based iterative control for hip extension assistance with a soft exosuit. *In Robotics and Automation (ICRA), 2016 IEEE International Conference*, pages 3501–3508, 2016.

[24] A. Young, J. Foss, H. Gannon, and D. Ferris. Influence of power delivery timing on the energetics and biomechanics of humans wearing a hip exoskeleton. *Frontiers in Bioengineering and Biotechnology*, 5, 2017.

[25] H. Herr. Exoskeletons and orthoses: classification, design challenges and future directions. *Journal of Neuroengineering and Rehabilitation*, 6(1):21, 2009.

[26] J. Hitt, et al. Dynamically controlled ankle-foot orthosis (DCO) with regenerative kinetics: Incrementally attaining user portability. *Proceedings of the 2007 IEEE International Conference on Robotics and Automation*, 1–10:1541–1546, 2007.

[27] H. Kawamoto, Y. Sankai. Power assist system HAL-3 for gait disorder person. *Computers Helping People with Special Needs*, pages 19–29, 2002.

[28] S. Diller, C. Majidi, and S. H. Collins. A lightweight, low-power electroadhesive clutch and spring for exoskeleton actuation. *IEEE International Conference on Robotics and Automation (ICRA)*, pages 682–689, 2016.

[29] G. Stefan, G. Rusticelli, A. Zucchelli, S. Stramigioli, and R. Carloni. The variable stiffness actuator vsaut-ii: Mechanical design, modeling, and identification. *IEEE/ASME Transactions on Mechatronics*, 19(2):589–597, 2014.

[30] S Arno, et al. Self-aligning exoskeleton axes through decoupling of joint rotations and translations. *IEEE Transactions on Robotics*, 25(3):628–633, 2009.

[31] B. Koopman, E. Asseldonk, and H. Kooij. Estimation of Human Hip and Knee Multi-Joint Dynamics Using the LOPES Gait Trainer. *IEEE Transactions on Robotics*, 32 (4):920–932, 2016.

[32] S. Pfeifer, H. Vallery, M. Hardegger, R. Riener, and E. J. Perreault. Model-based estimation of knee stiffness. *IEEE Transaction on Biomedical Engineering*, 59:2604–2612, 2012.

[33] S. Pfeifer, R. Riener and H. Vallery. Knee stiffness estimation in physiological gait. *Conference Proceedings IEEE Engineering in Medicine and Biology Society*, pages 1607–1610, 2014.

[34] K. Shamaei, G. Sawicki, and A. Dollar. Estimation of quasi-stiffness of the human hip in the stance phase of walking. *PLoS One*, 8(12):1–11, 2013.

[35] E. Rouse, R. Gregg, L. Hargrove, and J. Sensinger. The difference between stiffness and quasi-stiffness in the context of biomechanical modeling. *IEEE Transaction on Biomedical Engineering*, 60(2):562–568, 2012.

[36] J. Caputo and S. Collins. An experimental robotic testbed for accelerated development of ankle prostheses. *In Robotics and Automation (ICRA), 2013 IEEE International Conference*, pages 2630–2635, 2013.

[37] K. Witte, J. Zhang, R. Jackson, and S. Collins. Design of two lightweight, high-bandwidth torque controlled ankle exoskeletons. *In Robotics and Automation (ICRA), 2015 IEEE International Conference on*, pages 1223–1228, 2015.

[38] Y. Ding, I. Galiana, A. Asbeck, B. Quinlivan, S. De Rossi, and C. Walsh. Multi-joint actuation platform for lower extremity soft exosuits. *Robotics and Automation (ICRA), 2014 IEEE International Conference on*, pages 1327–1334, 2014.

[39] J. Caputo and S. Collins. A universal anklefoot prosthesis emulator for human locomotion experiments. *Journal of Biomechanical Engineering*, 136(3):035002, 2014.

[40] K. Samuel, P. Dilworth, and H. Herr. An ankle-foot emulation system for the study of human walking biomechanics. *Robotics and Automation, 2006. ICRA 2006. Proceedings 2006 IEEE International Conference on. IEEE*, pages 2939–2945, 2006.

[41] C. Fryar, Q. Gu, and C. Ogden. Anthropometric reference data for children and adults: United States, 20072010. *National Center for Health Statistics, Vital Health Stat*, 11 (252):1–40, 2012.

[42] F. Scheid. Outline of theory and problems of numerical analysis. *New York: McGraw-Hill, 1968*, 1968.

[43] R. Kearney and I. Hunter. System identification of human joint dynamics. *Critical Reviews in Biomedical Engineering*, 18(1):55–87, 1989.

[44] G. Agarwal and C. Gottlieb. Compliance of the human ankle joint. *Journal of Biomechanical Engineering*, 99:166, 1977.

[45] L. Ljung. System identification. : Wiley online library. *New York: McGraw-Hill, 1968*, 1968.

[46] S.J. Lee and J. Hidler. Biomechanics of overground vs. treadmill walking in healthy individuals. *Journal of Applied Physiology*, 104(3):747–755, 2008.
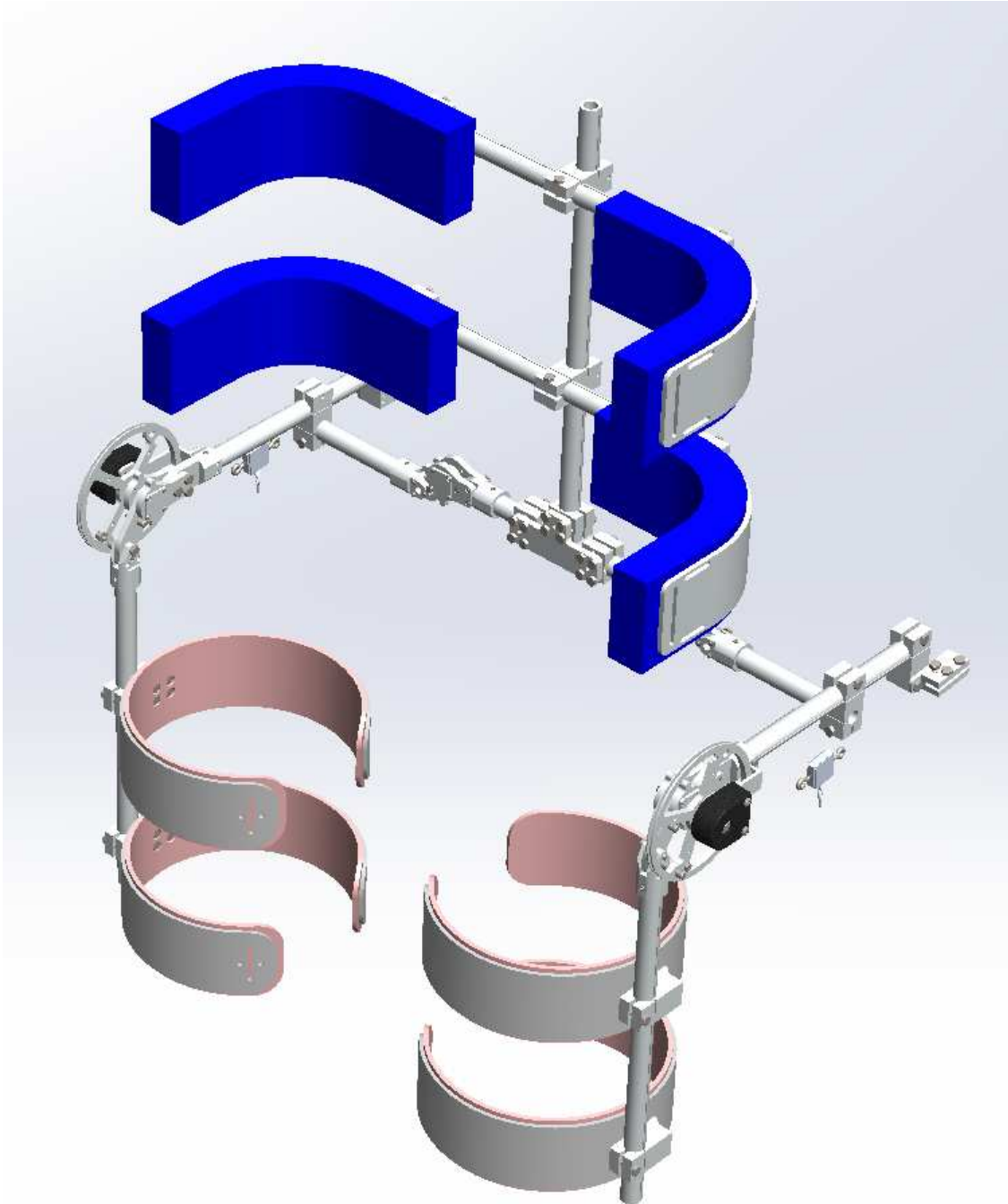
APPENDIX A

EXOSKELETON BRACE DESIGN

Figure 4.13: SOLIDWORKS Model of Hip Brace

Figure 4.14: SOLIDWORKS Model of Knee Brace

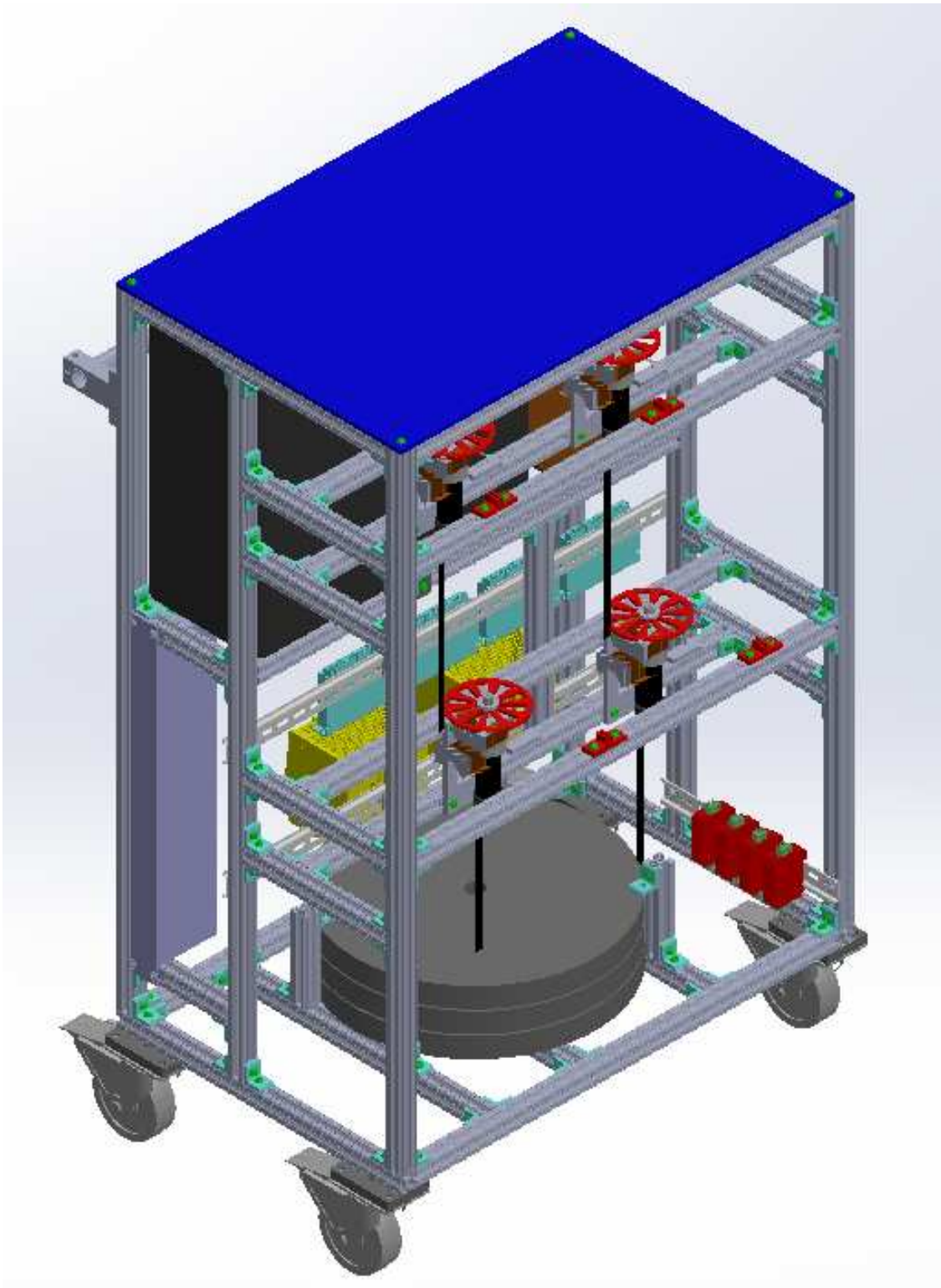Figure 4.15: SOLIDWORKS Model of Ankle Brace

Figure 4.16: (Isometric View) SOLIDWORKS Model of Actuation Cart
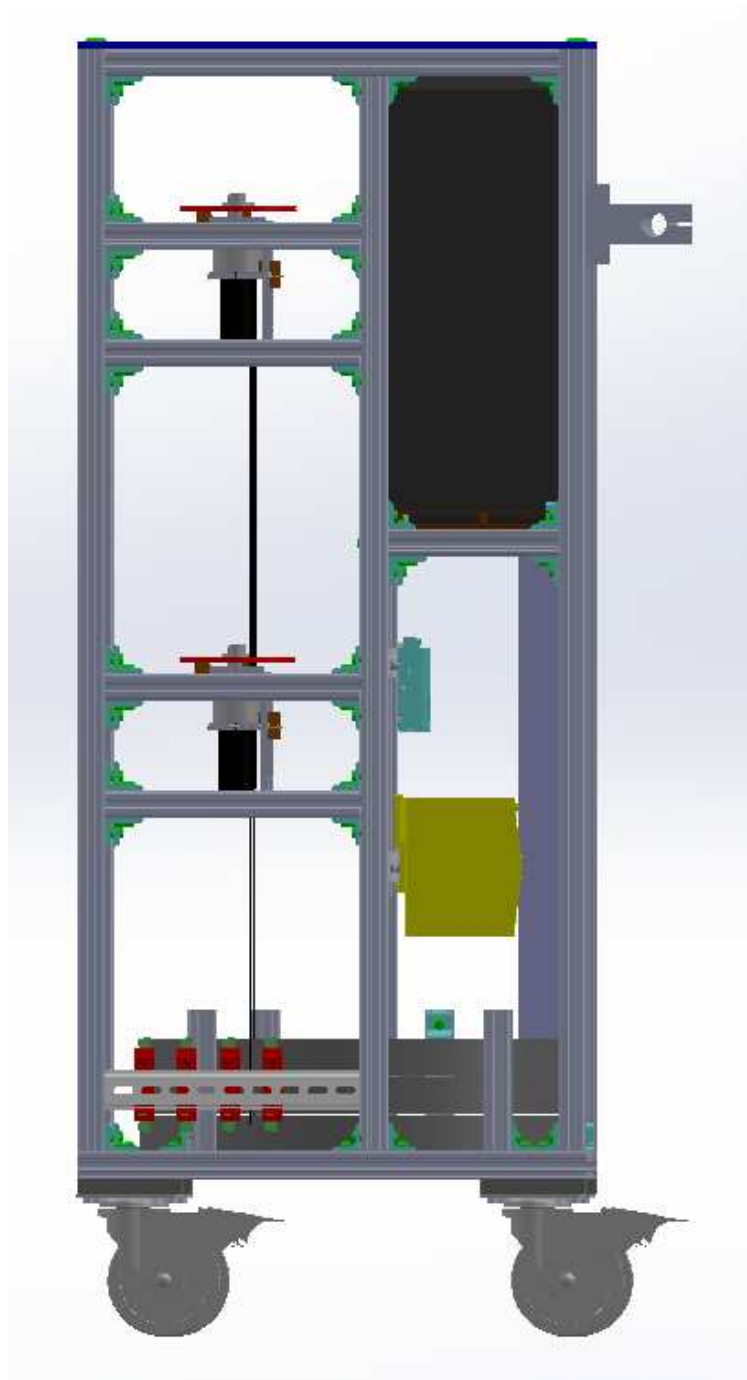Placement of stacked 45lbs weighted olympic plates is located at the bottom level.

Figure 4.17: (Side View) SOLIDWORKS CAD of Actuation Cart
The left side of the vertical column is the mechanical side (motors and pulleys). The right side of the vertical column contains the electronic side (desktop PC, data acquisition board, motor amplifiers, and power supplies).
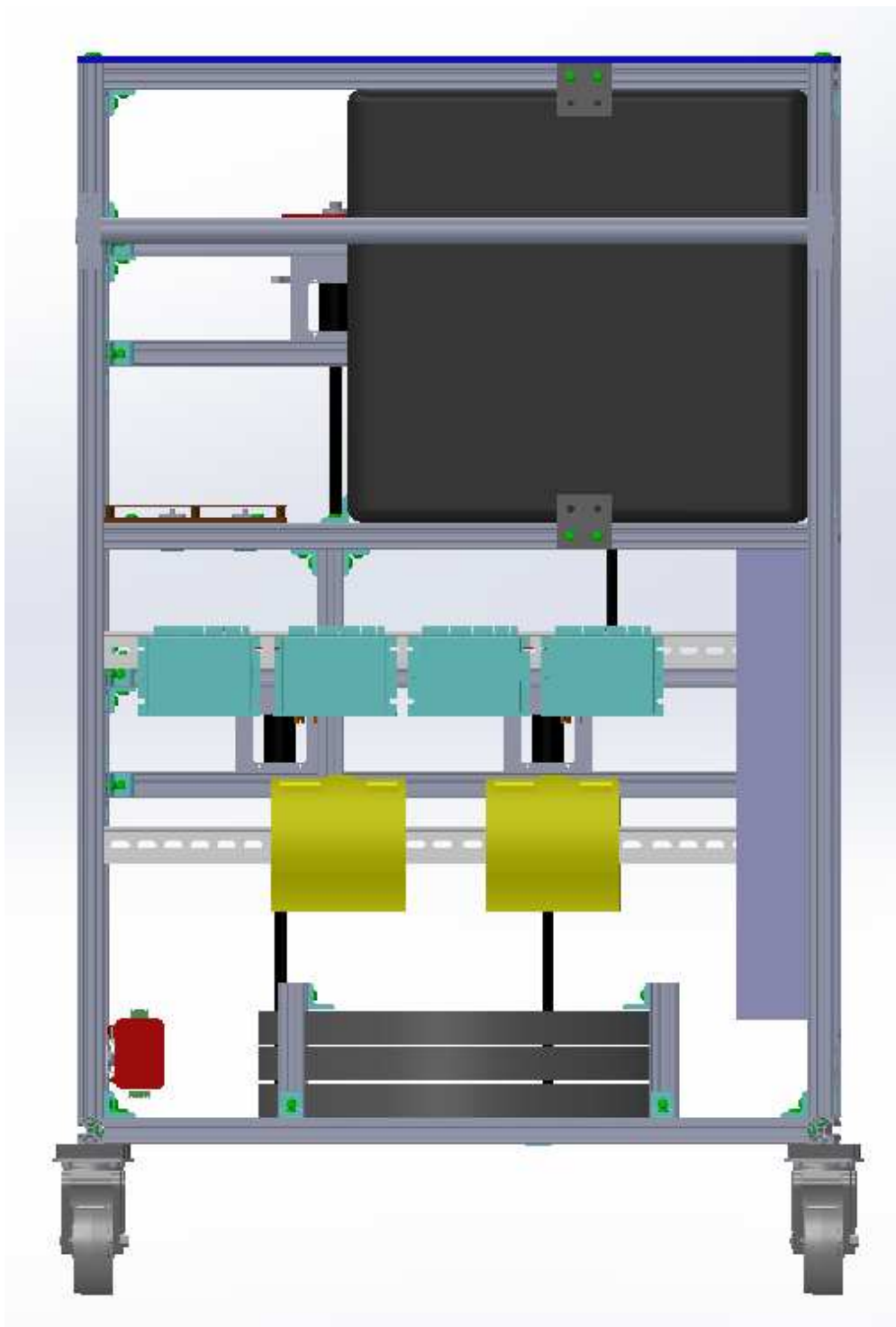
Figure 4.18: (Back View) SOLIDWORKS Model of Actuation Cart

APPENDIX B

EXPERIMENTAL SETUP
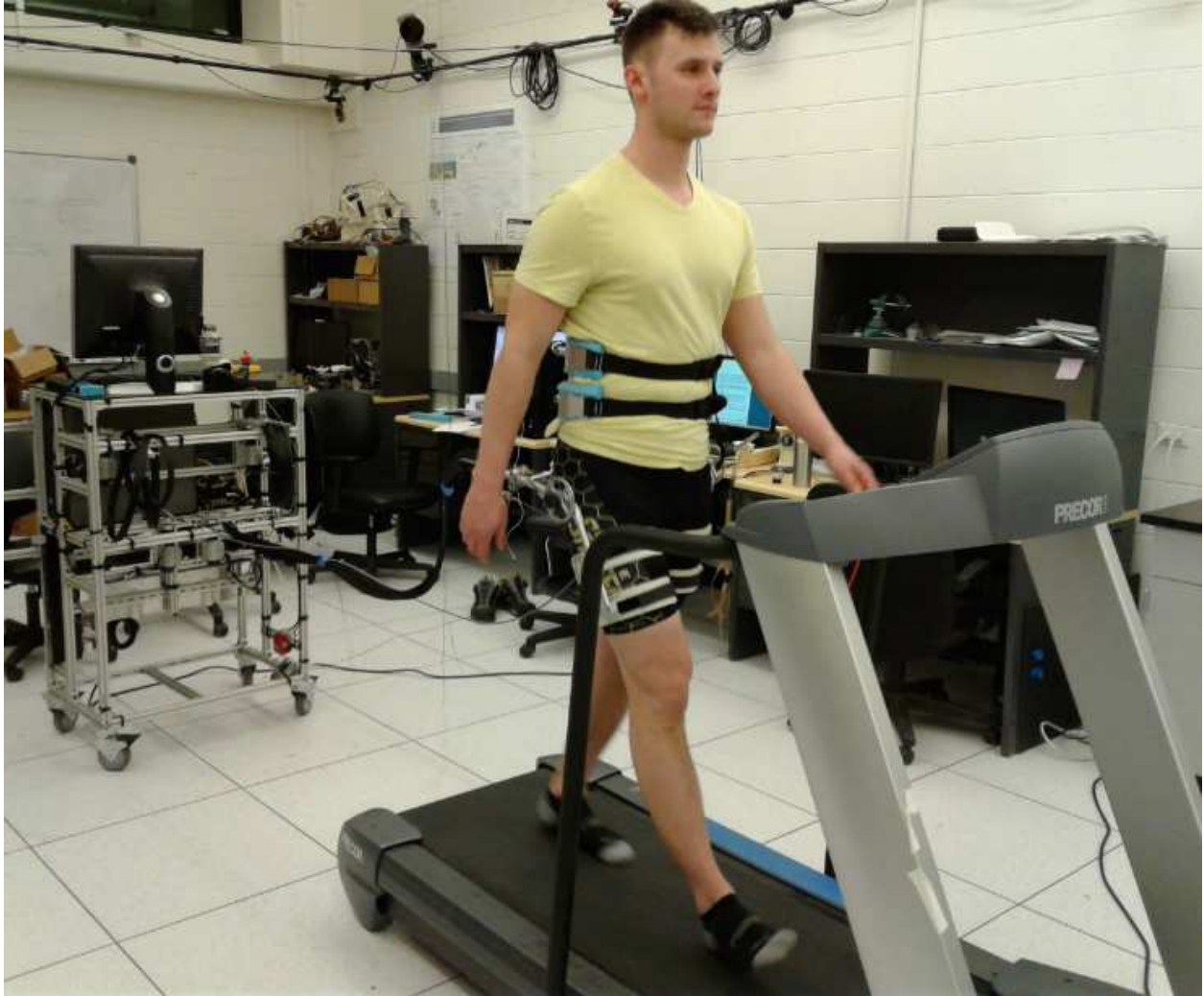
Figure 4.19: Iso-view of Hip Experimental Setup

APPENDIX C

DATA ANALYSIS
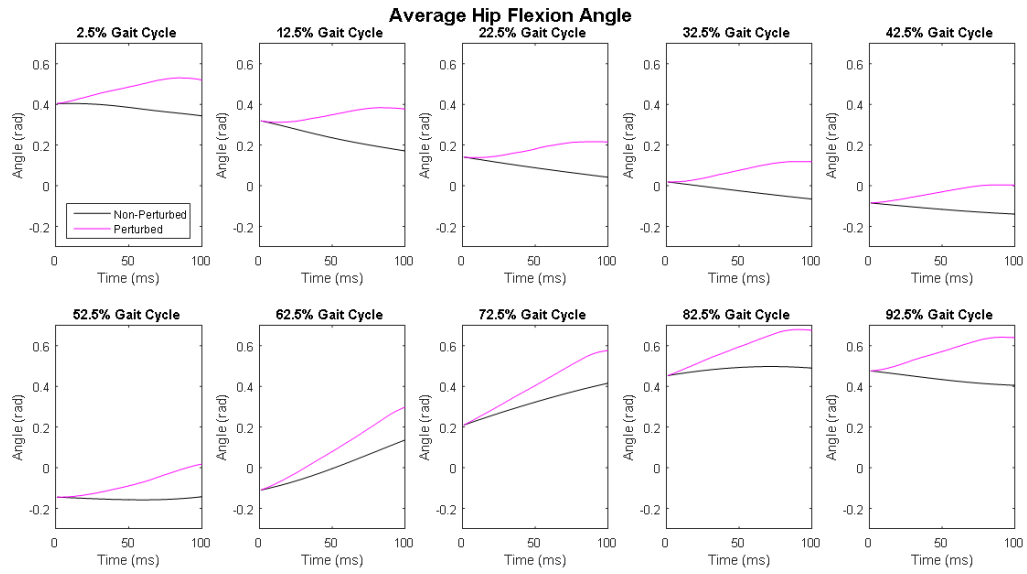
Figure 4.20: Average Hip Angle For all Perturbation Timings (Flexion Perturbations)
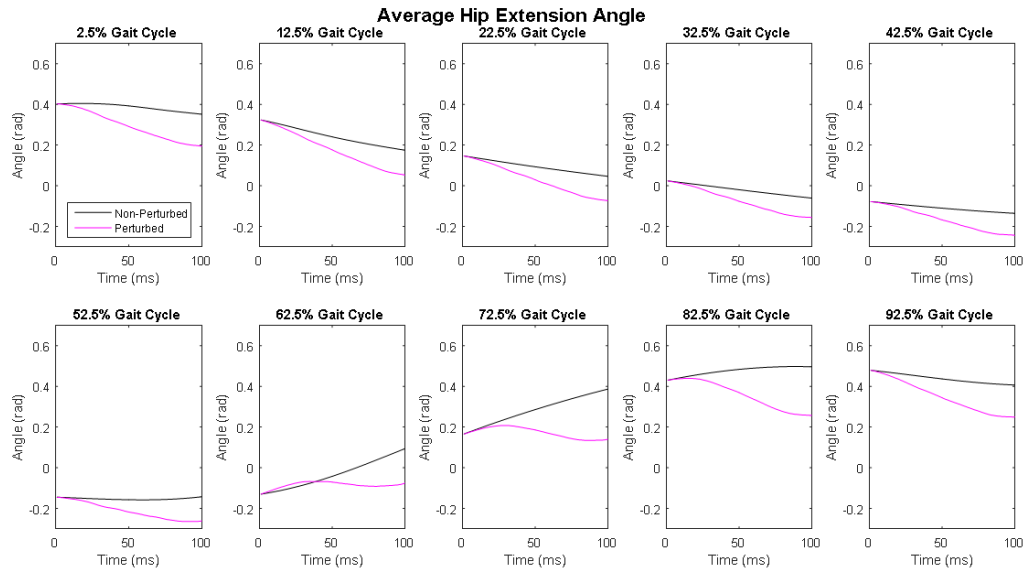
Figure 4.21: Average Hip Angle For all Perturbation Timings (Extension Perturbations)
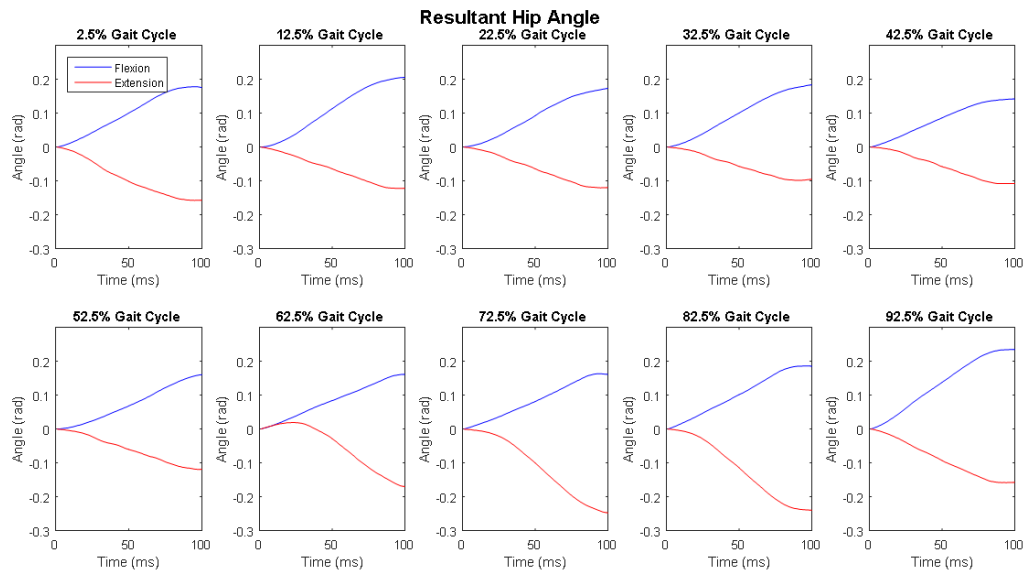
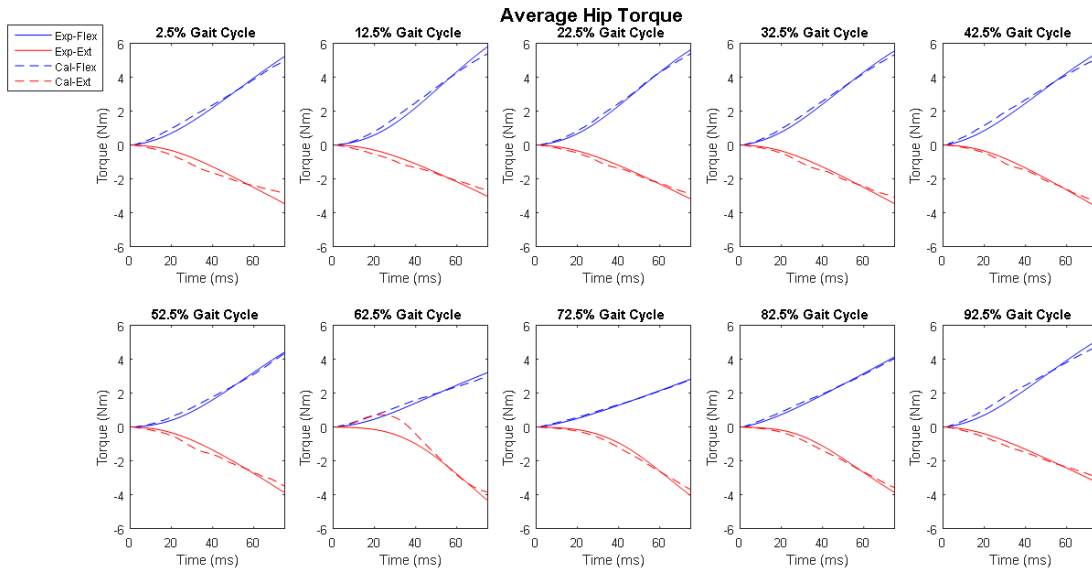Figure 4.22: Resultant Hip Angle For all Perturbation Timings

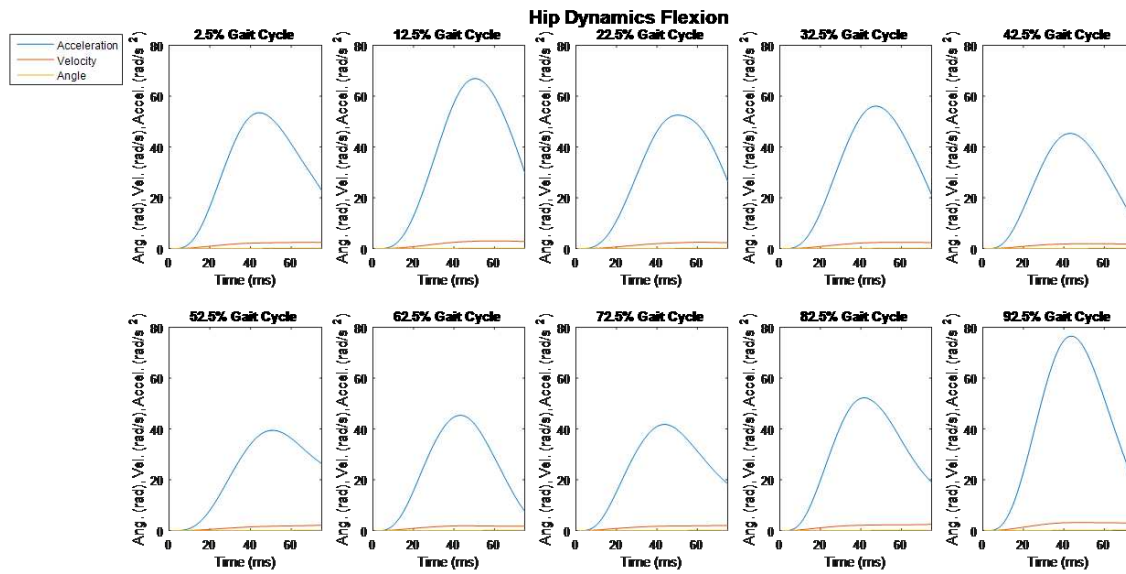Figure 4.23: Average Hip Torque For all Perturbation Timings

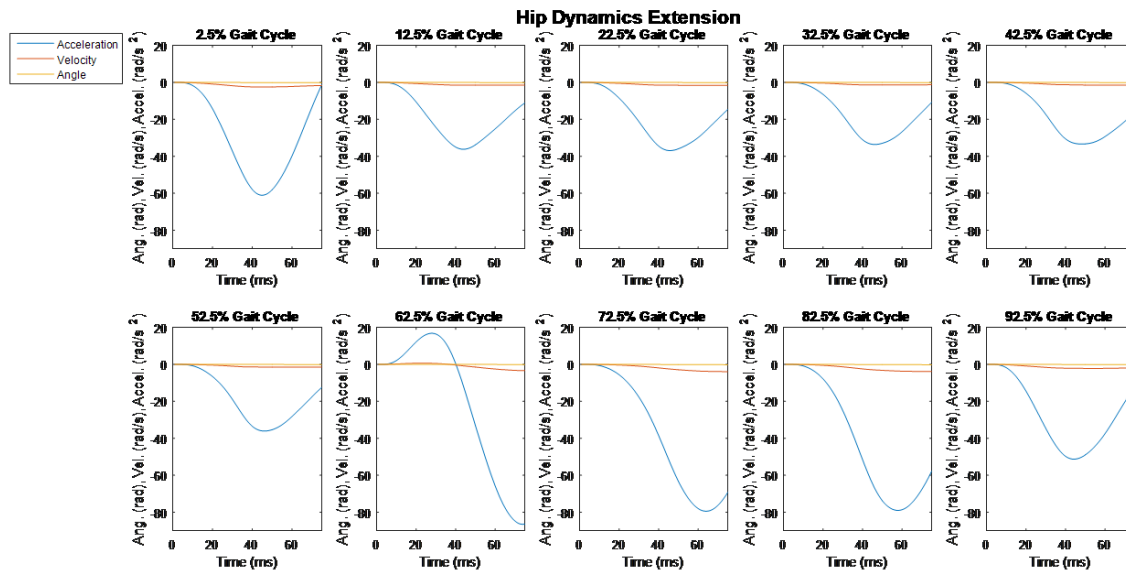Figure 4.24: Hip Dynamic Flexion For all Perturbation Timings

Figure 4.25: Hip Dynamic Extension For all Perturbation Timings